https://doi.org/10.5194/egusphere-2025-5528
Preprint. Discussion started: 4 December 2025

Evaluation of the vertical microphysical properties of fog as simulated by Meso-NH during the SOFOG3D experiment

Marie Mazoyer[1], Christine Lac[1], Frédéric Burnet[1], Benoît Vié[1], Marie Taufour[1], Théophane Costabloz[1], Salomé Antoine[1], and Maroua Fathalli[1]

[1]Météo-France, CNRS, Univ. Toulouse, CNRM, Toulouse, France.

Correspondence: M.Mazoyer (marie.mazoyer@meteo.fr)

Abstract. This study evaluates the representation of fog microphysics in high-resolution simulations from the Meso-NH model using the two-moment LIMA microphysical scheme, based on data from the SOFOG3D field campaign. This campaign combines remote sensing and vertical microphysical observations from a tethered balloon. Two fog events were simulated in order to assess the model's ability to reproduce their life cycle and identify any missing physical processes. The analysis focuses on the vertical microphysical structure, observed consistently by the various instruments, and on the simulated processes during the different phases of fog development (i.e. before, during, and after the transition from thin to thick fog). The model realistically reproduces the thermodynamic and dynamic evolution of fog, resulting in a satisfactory simulation of its development stages. A comprehensive analysis of microphysical processes is conducted throughout the entire height of the fog, based on a comparison with observations and a budget of modelled processes. While microphysics is generally well represented, certain systematic errors emerge: excessive liquid water content values vertically during the thin-to-thick transition and adiabatic phases, due to excessive condensation; an inaccurate representation of the droplet side distribution, with the absence of the largest droplets; and an inability to capture the droplet concentration vertical gradient, with values that are too high near the ground. While some of these shortcomings can be explained by dynamic biases, and more cases are needed to confirm our results, various recommendations are proposed. These include assessing the impact of drizzle and representations that could benefit all warm clouds.

Short summary. Fog modelling remains a significant challenge due to the complex, interrelated physical processes involved, including microphysics. We evaluated the ability of an advanced microphysical scheme within Meso-NH to reproduce the fog life cycle by comparing it with new vertical microphysical observations obtained using a tethered balloon during the SOFOG3D field campaign. Although realistic modelling performance was achieved, some biases remain that require further microphysics observations.

https://doi.org/10.5194/egusphere-2025-5528
Preprint. Discussion started: 4 December 2025

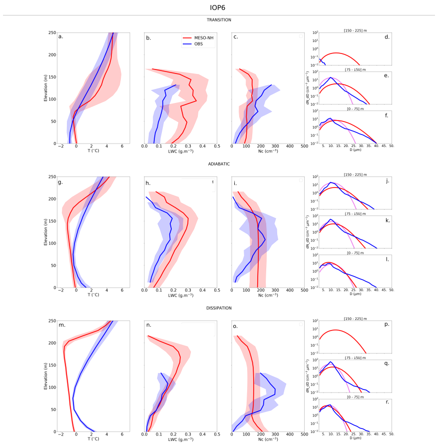

https://doi.org/10.5194/egusphere-2025-5528
Preprint. Discussion started: 4 December 2025

1 Introduction

Modeling fog is a significant challenge to forecasters. A key step towards achieving this is to understand the complex, interrelated physical processes that influence the fog life cycle. Fog results from the intricate interactions of local airflow, surface processes, radiation, turbulence, aerosol loading, and microphysics.

Numerous numerical studies have investigated the relationships between fog microphysics and other physical processes (see, for example, Zhang et al., 2014; Mazoyer et al., 2017; Boutle et al., 2021; Contreras Osorio et al., 2022). These studies emphasize the critical role of accurately representing Droplet Size Distribution (DSD) for sedimentation, radiative, and dynamic effects throughout the fog life cycle. However, even bin models, which are among the most accurate microphysical models, have struggled to capture this complexity (Boutle et al., 2021). In particular, the transition from thin fog to well-mixed thick fog remains poorly understood (Price, 2011; Bergot and Lestringant, 2019) and may be linked to microphysical processes. This transition occurs as the surface becomes radiatively shielded by the forming fog, causing the radiation inversion to shift upwards and thereby initiating a convective regime (Roach et al., 1976). In modeling scenarios, this shift tends to be too abrupt, often due to excessive fog droplet number concentration and liquid water content (Poku et al., 2021; Boutle et al., 2021). A numerical study by Boutle et al. (2018) suggested that aerosol growth and activation are crucial in triggering adiabatic fog.

Modeling these microphysical processes remains challenging (Boutle et al., 2018; Schwenkel and Maronga, 2019; Poku et al., 2021; Contreras Osorio et al., 2022; Vié et al., 2024), which has motivated the study of fog microphysics in field campaigns for many years (Gerber, 1991; Wendisch et al., 1998; Garcıa-Garcıa et al., 2002; Zhao et al., 2013; Price et al., 2018; Mazoyer et al., 2022; Ghude et al., 2023). Experimental field studies are essential to improve our understanding of fog microphysical processes and their modeling. Historically, measurements were primarily made near the ground for practical reasons. Data from numerous field campaigns indicate that, for diameters of 2–50 μm, surface droplet concentrations (Nc) near the ground range from 10 cm^{-3} to 300 cm^{-3}, with Liquid Water Contents (LWC) varying between 0.001 g.m^{-3} and 0.4 g.m^{-3}. The DSD has been documented as having undergone four evolutionary phases (formation, development from thin fog to well-mixed thick, mature and dissipation), driven by a combination of the following processes: activation, condensation, evaporation and sedimentation, while collision-coalescence or Ostwald ripening (when larger droplets grow at the expense of smaller ones) were only suspected. It has been shown that transitions between phases are linked to thermodynamics and radiation evolution (Mazoyer et al., 2022). However, little is known about microphysical properties in the fog layer as vertical measurements of fog microphysics using tethered balloons have a short history.

One of the aims of the LANFEX campaign (Price et al., 2018) was to investigate the vertical microphysical structure of fog using tethered balloon observations between September 2014 and March 2016. However, the scarcity of the profiles collected during LANFEX made documentation difficult. A few years later, the SOuth West FOGs 3Dimensions (SOFOG3D) campaign (Burnet et al., 2020) investigated the vertical microphysical structure of fog during the winter of 2019–2020 in South-West France using tethered balloon observations. The campaign employed a combination of in situ instrumentation and remote sensing to offer a thorough evaluation of fog events. SOFOG3D provided a valuable opportunity to analyze the vertical and temporal evolution of various fog layers.

So far, initial vertical measurements could not investigate the fog life cycle as they corresponded to isolated profiles within the fog layer, and they produced apparently contradictory results. While Goodman (1977); Pinnick et al. (1978) showed DSD broadening with height, other studies from Okita (1962); Pilié et al. (1975); Egli et al. (2015) reported DSD narrowing with height. These results may be explained by the timing of the measurements (before, during, or after the transition from thin to well-mixed thick fog), as demonstrated by Dione et al. (2023); Costabloz et al. (2024) for LWC using SOFOG3D measurements. By analyzing 140 vertical profiles of liquid water content (LWC) measured during this campaign, Costabloz et al. (2024) showed the following trend; before the transition, high LWC values are concentrated near the bottom; during the transition, higher amounts are found near the top as the temperature profile becomes unstable; and in the mature adiabatic phase after the transition, high LWC values are typically found near the fog top. However, these strong values at the fog top can be disrupted by entrainment-mixing processes, which reduce fog adiabaticity. The authors demonstrated that the transition is strongly linked to an increase in fog optical thickness, which is related to DSD. According to these authors, collision-coalescence and sedimentation may redistribute the LWC through the fog layer from the top to the ground, thereby balancing the described trend.

Modelling can provide additional insight into the microphysical processes that occur during the fog life cycle. Accurate prediction of the fog life cycle is also challenging. This requires the use of a two-moment microphysical scheme that considers prognostic droplet concentration in addition to mixing ratio, as demonstrated by Ducongé et al. (2020); Fathalli et al. (2022); Antoine et al. (2023); Vié et al. (2024) among others. However, these schemes still exhibit inaccuracies and therefore require specific validation for fog. To improve fog representation, recent modeling studies have consequently focused on aerosol activation schemes, which parameterize the droplet number concentration based on a change in supersaturation at a given time. However, initial supersaturation calculations, inherited from convection studies, only consider adiabatic lifting and many impose a minimum vertical velocity (e.g. $0.1\,\mathrm{m\,s^{-1}}$) to account for the unresolved subgrid ascent. According to Poku et al. (2021), fog's optical thickness is overestimated due to excessive aerosol activation during formation whereas at this time, supersaturation should be driven by non-adiabatic processes such as radiative cooling. This leads to overly intense convective regimes and a feedback loop of high activation and LWC production. They show that reducing the minimum vertical velocity and including radiative cooling in the supersaturation calculation slows the transition from thin to well-mixed thick fog. However, they also state that physical processes should be missing. In addition to Poku et al. (2021), Vié et al. (2024) also accounted for condensation on pre-existing cloud droplets as a sink term in the supersaturation equation. They demonstrated that fog development was slower, and that the supersaturation values were very close to those obtained using the reference but costly semi-prognostic scheme of Thouron et al. (2011). However, these two studies were based on the LANFEX campaign, which observed a limited number of microphysical vertical profiles.

The analysis of DSD evolution can also provide valuable insights into the microphysical processes at work. In a bulk scheme, the DSD is given by a distribution law, whose parameters depend on LWC and Nc for a two-moment microphysical scheme. Additionally, LWC and Nc represent the first- and third-order moments of the DSD, respectively. But, the evolution of the observed DSD is far more complex. The evolution of each DSD bin in the commonly observed diameters of 2–50 μm may result from different processes. Following Mazoyer et al. (2019, 2022), the growth of the 10 μm small-diameter mode results

https://doi.org/10.5194/egusphere-2025-5528
Preprint. Discussion started: 4 December 2025

from the activation of aerosol particles into droplets. Its condensation growth would feed small- to medium-sized droplets (up to 30 μm in diameter). For larger diameters, as stated by Yau and Rogers (1996), their growth must result from other processes, as the timescale for condensation growth is longer than their appearance in fog (see also Mazoyer et al. (2022)). Several hypotheses can explain the presence of droplets larger than 30 μm in diameter, including collision-coalescence (Beard and Ochs III, 1993; Pinsky et al., 2001), which can be gravitational or due to turbulence (Grabowski and Wang, 2013; Vaillancourt and Yau, 2000) especially at the fog top. Further investigations based on both observation and modelling are still needed to better understand the microphysical processes responsible for the evolution of the DSD.

This study aims to evaluate the two-moment microphysical scheme LIMA (Vié et al., 2016) with the supersaturation equation developed in Vié et al. (2024) within the Meso-NH model (Lac et al., 2018), using high-resolution mesoscale simulations and the SOFOG3D observations to evaluate fog microphysics. Notably, Meso-NH is the research laboratory for the French operational model AROME (Seity et al., 2011; Brousseau et al., 2011, 2016), which may integrate the LIMA microphysical scheme in the near future. This study will focus on radiation/advection fog during Observation Periods (IOP) 6 and 11 of the SOFOG3D campaign, which have been well documented in Dione et al. (2023); Costabloz et al. (2024). Microphysical assessments will be conducted according to the four evolutionary phases (formation, transition from thin,to thick, mature adiabatic phase and dissipation) outlined in Mazoyer et al. (2022) and Costabloz et al. (2024). A budget analysis of simulated LWC and droplet concentration (Nc), combined with an analysis of DSD evolution, will be performed to identify the primary microphysical processes involved in these phases, and to evaluate their representation in LIMA.

To the authors' knowledge, this is the first study to evaluate simulated vertical microphysical profiles alongside observations throughout the fog life cycle. The study addresses the following questions :

- To what extent is the fog life cycle, especially the vertical microphysical profiles (LWC, droplet concentration, DSD, and reflectivity), accurately represented using the two-moment microphysical scheme LIMA, particularly in light of the recent improvements to the treatment of supersaturation?
- Which microphysical processes, if any, are still missing from the representation, and how could the model be improved?

The paper is structured as follows: Section 2 describes the instrumental setup, observed cases, and model characteristics. Section 3 evaluates the simulations by comparing them with thermodynamic and dynamic measurements. Section 4 outlines the methodology for determining the transition from thin to well-mixed thick fog and different fog phases. Section 5 compares model simulations with tethered balloon data regarding microphysics and analyzes the main simulated microphysical processes. Sections 6 and 7 provide discussion and conclusions, respectively.

2 Case description and methodology

2.1 SOFOG3D Measurements set-up

The SOFOG3D field experiment (Burnet et al., 2020) took place in southwestern France, as illustrated in Figure 1, which shows the geographical location of the campaign at the edge of the Landes forest, an area characterized by a heterogeneous orography between two river valleys. Conducted during the autumn and winter of 2019-2020, the campaign included 15 Intensive Observation Periods (IOPs), and its dataset has been extensively analyzed in previous studies (Martinet et al., 2022; Antoine et al., 2023; Dione et al., 2023; Thornton et al., 2023; Costabloz et al., 2024; Price, 2025).

Measurements were collected at 17 sites over an area of 30 x 50 km^2 (larger rectangle of Fig. 1a), but this paper focuses on data from a denser 10 x 10 km^2 region surrounding the supersite, which includes Jachère and Charbonnière—the most instrumented sites (Fig. 1b). Both sites were equipped with ground-based meteorological stations that provided standard measurements, including temperature, wind speed and direction, and longwave and shortwave radiation. The Jachère site also provided flux measurements, particularly turbulent kinetic energy and vertical wind variance.

A distinctive feature of the SOFOG3D campaign was its profiling capabilities, which combined remote sensing and in situ measurements. At the Charbonnière site, the 95 GHz BASTA vertical cloud radar (Delanoë et al., 2016) measured droplet reflectivity and Doppler velocity up to 18 km, with a vertical resolution of 12.5 m. The Cloud Top Height (CTH) was derived from the reflectivity data. In addition, a HATPRO 1/10 Hz radiometer was deployed at Charbonnière, using neural network inversion (Martinet et al., 2022) to measure vertical profiles of temperature and humidity up to 2.5 km, with a vertical resolution of 25 m at lower altitudes and 30 m at higher altitudes. Note that Martinet et al. (2022) estimated a 0.5 K cold bias below 2 km and a 1.4 $g.m^{-3}$ dry bias below 1.7 km when comparing HATPRO measurements with RS data. The radiometer also retrieved the Liquid Water Path (LWP) for the entire atmospheric layer with errors between 1 and 14 $g.m^{-2}$ according to Martinet et al. (2022). A WindCube V2 lidar manufactured by Leosphere provided the wind measurements at 10 levels from 40 m to 220 m a.g.l at the Charbonnière site. The measurements, made at a frequency of 1 Hz and a vertical resolution of 20 m, allow for the estimation of turbulence parameters such as Turbulent Kinetic Energy (TKE). In the presence of fog or low stratus, the vertical range of the lidar decreases. WindCube lidar data are presented in more details in Dione et al. (2023). Furthermore, a tethered balloon equipped for microphysical measurements was deployed at the Charbonnière site, using a modified Cloud Droplet Probe (CDP) to collect data. The CDP measures DSDs ranging from 2 to 50 μm in diameter. More details on the CDP under the tethered balloon can be found in Fathalli et al. (2022); Dominutti et al. (2022); Costabloz et al. (2024).

Instrumentation at the Jachère site was set up to assess the aerosol load and its activity as Cloud Condensation Nuclei (CCN). This included a continuous flow streamwise thermal gradient CCN chamber (CCNC) (Roberts and Nenes, 2005), which measured CCN number concentration at five different supersaturations ranging from 0.06% to 0.28%. A Scanning Mobility Particle Sizer (SMPS) provided the number size spectrum of dry aerosol particles. The SMPS consisted of a differential mobility analyzer (DMA; TSI 3071), which selected particles from 10.6 to 496 nm, paired with a Condensation Particle Counter (TSI CPC 3022).

A summary of the instruments used in this study is presented in Table 1.

2.2 SOFOG3D case studies

This study examines two fog events observed during IOPs at the SOFOG3D supersite.

During the IOP 6, the fog formed on 5 January 2020 at 20:37 UTC and dissipated on 6 January 2020 at 09:28 UTC under high-pressure conditions associated with a strong anticyclone over central Europe, and lasted 12 hours and 51 minutes. Satellite images (not shown) indicated low-level cloud advection at 20:00 UTC: the fog was classified as radiative by the Tardif and Rasmussen (2007) algorithm but as a radiative-advective fog according to Costabloz et al. (2024).

In contrast, IOP 11 was a radiative fog (Costabloz et al., 2024) that formed at 20:38 UTC on 8 February 2020 and dissipated at 03:49 UTC on 9 February 2020, lasting 7 hours and 11 minutes. This fog developed after the passage of a cold front earlier in the day, but its persistence was disrupted by the arrival of high clouds at 04:00 UTC on 9 February, leading to its dissipation before sunrise (satellite images not shown).

The Hybrid Single-Particle Lagrangian Integrated Trajectory (HYSPLIT, Draxler and Rolph (2010)) model suggests that the air masses during IOP 6 were of continental origin, whereas those during IOP 11 were of maritime origin (data not shown). Due to technical issues, aerosol measurements were not available for these dates.

2.3 Model set-up

The non-hydrostatic research model Meso-NH (Lac et al., 2018) is used in a 3D high-resolution configuration (Cuxart, 2015), which has proven effective for fog simulations (Ducongé et al., 2020; Fathalli et al., 2022). Simulations were performed over a 48-hour period, starting on 5 January at 00 UTC for IOP 6 and on 8 February at 00 UTC for IOP 11. Fields from the AROME model (Seity et al., 2011; Brousseau et al., 2011), with a 1.3 km horizontal grid, were used as initial and boundary conditions with the configuration previously identified as the most satisfactory: AROME analyses for IOP 6, and AROME-IFS forecasts for IOP 11. AROME-IFS refers to an AROME configuration in dynamical adaptation from Integrated Forecasting System (IFS), i.e., initialized with IFS analyses and coupled with IFS forecasts.

The parent domain has a 500 m horizontal resolution, covering a 150 km x 90 km area (Fig. 1a). Within this domain, a nested 100-m horizontal grid model spans 60 km x 40 km and is centered on the main observation site. Both nested domains use 138 vertical levels, extending from the ground to the model top at 10 km, with vertical grid spacing ranging from 2 m near the ground to 500 m at the model ceiling. A nudging technique is applied to large-scale dynamical and thermodynamic fields above 9 000 m above sea level, using an absorbing layer to relax forecast variables toward large-scale conditions.

For momentum variables, a fourth-order centered advection scheme is employed, along with a fourth-order Runge-Kutta time integration. Scalar variables are transported using the piecewise parabolic scheme (Colella and Woodward, 1984).

The atmospheric model is coupled to the soil-biosphere-atmosphere interaction surface scheme (Noilhan and Planton, 1989) through the externalized surface model SURFEX (Masson et al., 2013). Orography data come from the Shuttle Radar Topography Mission, providing a resolution of 90 m for the 500 m model and 30 m for the 100 m model. Land cover and surface parameters are derived from the ECOCLIMAP database at 1 km resolution. The turbulence scheme is based on a turbulent kinetic energy equation (Cuxart et al., 2000), implemented in one-dimensional mode with the Bougeault and Lacarrere (1989) mixing length for the 500 m grid, and in three-dimensional mode with the Deardorff (1980) mixing length for the 100 m grid, both of which are well-suited to these resolutions. At 500 m grid length, subgrid condensation is activated. It depends on the parameters computed by the turbulence scheme and a climatological variance (Rooy et al., 2010; De Rooy et al., 2022) associated with a critical relative humidity of 96%. At the 100 m grid length, no subgrid condensation scheme is required. In the following parts, we will only consider the 100 m simulated fields.

https://doi.org/10.5194/egusphere-2025-5528
Preprint. Discussion started: 4 December 2025

The microphysical scheme used is the two-moment Liquid Ice Multiple Aerosol (LIMA) scheme (Vié et al., 2016), which prognoses the mixing ratios of five hydrometeor species (cloud droplets, cloud ice, snow, rain, and graupel) and the concentrations of droplets, raindrops, and ice crystals. LIMA also accounts for the evolution of the aerosol population, providing a detailed representation of aerosol-cloud interactions to address competition between multiple CCN modes. Each CCN mode is characterized by its chemical composition, size distribution, and nucleation properties. The parameterization of CCN activation, based on the maximum supersaturation diagnosis (Cohard and Pinty, 2000), considers vertical velocity (including a contribution from TKE), cloud droplet growth by condensation, and radiative cooling. Recent improvements in the CCN activation parameterization in LIMA, as developed in Vié et al. (2024), take into account the growth of existing cloud droplets by condensation, thereby mitigating the overestimation of cloud droplet activation. The rain formation rate in LIMA is determined by the cloud droplet size distribution following Berry and Reinhardt (1974) and Cohard and Pinty (2000). Droplet sedimentation is calculated using the Stokes law for cloud droplets, while fog deposition is activated with a constant velocity of 2 cm/s according to Mazoyer et al. (2017). LIMA assumes that the cloud droplet size distribution $nc(D)$ follows a generalized gamma law:

$$nc(D) = N_c \frac{\alpha}{\Gamma(\nu)} \lambda^{\alpha\nu} D^{\alpha\nu-1} exp(-(\lambda D)^{\alpha}) \tag{1}$$

where λ is the slope parameter, depending on the prognostic variables r_c (cloud mixing ratio, kg/kg) and N_c (cloud droplet concentration, cm^{-3}):

$$\lambda = (\frac{\pi}{6}\rho_w \frac{\Gamma(\nu+3/\alpha)}{\Gamma(\nu)} \frac{N_c}{\rho_a r_c})^{1/3} \tag{2}$$

ρ_a and ρ_w are the density of dry air and water, and α and ν are the parameters of the gamma law. These parameters used for both microphysics and radiation are set to α = 3 and ν = 1 within LIMA.

To specify aerosol loading, the characteristics of the activation spectra Cohard and Pinty (2000) were calculated according to the κ-Köhler theory (Petters and Kreidenweis, 2007) implemented in LIMA, using all data collected during the campaign with the SMPS (aerosol size distribution from 10.6 to 496 nm) and the CCNC (activation spectra from 0.06 % to 0.28 %), following the methodology in Mazoyer et al. (2019). The mean activation spectra obtained during SOFOG3D were found to be consistent with the Paris-Fog data (Mazoyer et al., 2019), with values of 80 cm^{-3} at 0.05 %, 250 cm^{-3} at 0.1 % and 1000 cm^{-3} at 0.3 % (not shown).

To compute model reflectivity offline, this study employs the radar forward operator developed by Augros et al. (2016). This forward operator accounts for hydrometeor and water vapour attenuation and is based on the T-matrix scattering theory (Mackowski and Mishchenko, 1996). Its implementation within Meso-NH has been previously described in Mazoyer et al. (2023).

The radiation code used in this study is ecRad (Hogan and Bozzo, 2018), with the Rapid Radiation Transfer Model (RRTM, Mlawer et al. (1997)) as the longwave (LW) radiation scheme, and 14 bands for the SW radiation. Cloud optical properties

https://doi.org/10.5194/egusphere-2025-5528
Preprint. Discussion started: 4 December 2025

are computed according to Savijärvi et al. (1997) with the LIMA scheme by taking into account the prognostic cloud droplet concentration. Note that the radiative effect of aerosols is not considered in these simulations.

3 Thermodynamic and dynamic evaluation by comparison to measurements

This section evaluates the simulated fog event by comparing it with thermodynamic and dynamic measurements. The objective is to assess the consistency of the subsequent detailed microphysical comparisons.

In order to evaluate the fog life cycle and its physical characteristics, we first compare observed and simulated vertical reflectivities. Next, we analyze the vertical profiles of the thermodynamic fields using radiosoundings (RS), alongside data from the HATPRO radiometer and wind lidar for the dynamic fields.

3.1 RADAR evaluation

Figure 2 compares the simulated radar reflectivity and LWP with the CDP observations under the tethered balloon and the BASTA radar observations and LWP from HATPRO at Charbonnières for IOPs 6 and 11, using a vertical logarithmic scale. Please note that comparisons of reflectivity derived from CDP and measured by the BASTA radar will be treated in section 5.

For IOP 6, the observed fog from radar formed at 20:38 UTC and rapidly developed vertically, reaching 100 m by 21:30 UTC. The fog top subsequently lowered until 00:00 UTC due to the wind shifting from southwest to southeast, and then continued to develop progressively until 04:00 UTC, finally dissipating as stratus by 09:00 UTC. High reflectivity values (around -20 dBZ) were recorded between 02:00 and 05:00 UTC with the BASTA. While the observed BASTA reflectivity values varied over time, they remained fairly homogeneous vertically. Costabloz et al. (2024) classified this episode as radiative-advective fog, because advection from the west maritime area favored the formation of fog in addition to radiative cooling near the ground. The simulated fog for IOP 6 exhibited a similar fog development, although discrepancies are noted. Notably, the simulation did not capture a thin fog layer before 22:00 UTC. The advective contribution to fog formation in the simulation appeared to be dominant over local formation, as fog first appeared at a height of 100 m at 22:00 UTC, before lowering abruptly. After formation, the simulated fog developed vertically to 250 m before lowering again and evolving into a stratus layer by 09:00 UTC, which is in close agreement with the observation. However, lower reflectivity values were simulated when the fog vertically extended, and the simulated vertical reflectivity gradient did not match the BASTA observations well. It is important to note that the strong radar reflectivities in the surface boundary layer after 09:00 UTC corresponds to minimal rain formation below the stratus. The simulated LWP values were generally higher, however both observed and simulated values reached up to 50 g.m^{-3}, but at 04:00 UTC in observations and 02:00 UTC in the simulation. The lower reflectivity despite higher simulated LWP could be attributed to potential inaccuracies in the simulated DSD with an underestimation of large droplets, as the reflectivity is proportional to the sixth order moment of the DSD. This point will be explored in more detail later on.

For IOP 11, the observed fog from radar formed at 20:38 UTC and was classified as a radiative fog by Costabloz et al. (2024), considering only its formation, which was primarily driven by significant radiative cooling near the ground. The fog then developed progressively until 04:00 UTC, when the first high clouds, indicative of an approaching warm front, appeared at

https://doi.org/10.5194/egusphere-2025-5528
Preprint. Discussion started: 4 December 2025

10,000 m. As the advection became a major process during its life cycle, Dione et al. (2023) classified IOP 11 as an advection-radiation fog. A reverse vertical reflectivity gradient, with the highest values near the ground, was observed with the BASTA until 03:00 UTC, suggesting the presence of large droplets near the bottom and a coalescence signature (Kumjian and Prat, 2014). From 03:00 UTC, the highest reflectivity values were recorded near the fog top, with the observed LWP reaching up to 45 g.m^{-2}. The simulation for IOP 11 was in good agreement with the BASTA observations in terms of fog development until 04:00 UTC. However, when examining the vertical reflectivity profile, simulated reflectivity values were significantly higher than observed, correlating with higher simulated LWP. After 04:00 UTC, high clouds were also simulated, but they were likely too thin, and the fog too thick, leading to a delayed fog dissipation in the simulation - occurring only at 09:00 instead of 04:10 UTC as observed.

Overall, despite discrepancies in reflectivity intensity and vertical profile, the fog evolution as inferred from reflectivity is generally consistent with observations for both IOP 6 and IOP 11 in the period after formation for IOP 6 and up to 04:00 UTC for IOP 11. We will focus on these periods in the following sections.

3.2 Thermodynamics and dynamic evaluation

3.2.1 Radiosoundings

In order to distinguish between model errors linked to thermodynamical and dynamical conditions and those linked to microphysics, Figure 3 compares the RS profiles of potential temperature and vapour mixing ratio (dotted lines), launched at Charbonnières, with the vertical profile simulated by Meso-NH (solid lines) at the same time. In addition, we include the vertical profiles from the coupling model (dashed lines), using temporally interpolated analyses from AROME for IOP 6 and forecasts from AROME-IFS for IOP 11, to assess the influence of the Meso-NH simulations. The vertical dashed lines in Figure 2 indicate the launch times of the RS and the simulated profiles, allowing us to examine the coincident vertical evolution of the fog.

For IOP 6, at 18:00 UTC, the stable boundary layer and surface cooling show that Meso-NH and AROME were not cold and dry enough in the surface layer compared to the RS data. By 21:43 UTC (blue lines in Figures 2 and 3), when both the observed and modeled fog layers became adiabatic, the coupling model closely aligned with the RS, although Meso-NH remained slightly warmer and wetter, retaining a higher water vapour content. This is consistent with the delayed fog formation in Meso-NH, which occurred at 22:00 UTC, later than in the observations (Fig 2a.b.). At 03:43 UTC, when the fog reached its maximum vertical development, the adiabatic potential temperature profiles were quite similar, although always slightly colder in the observations. In the same way, the observed fog layer was higher, consistent with Fig. 2a,b. By 09:19 UTC, the model simulated a more developed fog than observed, but the profiles remained very similar beneath the inversion.

For IOP 11, small differences between the observations, Meso-NH, and AROME-IFS are apparent from 18:00 UTC but they are quite small, and explain why fog formation was almost correctly reproduced, unlike in IOP 6. These differences persisted throughout the simulation. Meso-NH appeared cooler and drier, while AROME-IFS was warmer and wetter than the observations. The discrepancies observed at 22:33 UTC between the RS and Meso-NH may be due to the more developed simulated fog. By 05:36 UTC, after the first disturbances from the approaching warm front arrived, the profiles show similar trends. Notably, for this IOP, stable profiles were observed and modeled at 17:59 UTC and 22:33 UTC, whereas a quasi-adiabatic profile was observed and modeled only at 05:36 UTC, indicating a more progressive thin-to-thick transition than during IOP 6.

Overall, Meso-NH exhibits some discrepancies relative to its coupling model AROME, highlighting the specific influences of its configuration (such as the vertical grid) and physical parametrizations, in addition to the different dynamics. A precise analysis of the causes of the differences is beyond the scope of this study. Nevertheless, the simulated vertical profiles of potential temperature and vapour mixing ratio appear to be consistent with the observed RS data, in terms of absolute values and inversion level throughout the fog life cycle, for both IOP 6 and IOP 11, lending confidence to the thermodynamic representation of these fog events. It should be noted, however, that the simulation biases differ between the two IOPs: the model is generally too warm and too moist for IOP 6, while it is too cold and too dry for IOP 11.

3.2.2 Radiometer and lidar

Figures 4 (IOP 6) and 5 (IOP 11) show the temporal and vertical temperature profiles measured by the HATPRO radiometer, alongside wind profiles and turbulent kinetic energy (TKE) recorded by lidar. Radiosounding measurements are also included for temperature, wind and vapour mixing ratio. The simulated fields from Meso-NH are compared, with the simulated TKE field including resolved and subgrid energy. It is important to note that lidar wind and TKE measurements are subject to strong attenuation due to fog droplets, from bottom to top, which limits the vertical measurement.

For IOP 6, HATPRO observations suggest temperatures that are slightly warmer than those indicated by RS data within the fog layer. The simulated temperatures are slightly cooler than those from HATPRO and fall between the RS and HATPRO temperature measurements. The fog top is also more pronounced in the model than in HATPRO observations, primarily due to the lower vertical resolution of the measurements. Simulated winds below 150 m show fairly good agreement with lidar wind measurements, supporting their use for analyzing the dynamic characteristics of the fog layer. The simulated profiles of temperature, water vapour mixing ratio, and wind highlight a warm and dry low-level southerly jet, starting after 00:00 and intensifying above 200 m from 06:00 UTC onward. This jet likely contributes to the slight lowering of the fog top at 06:00 UTC. Observed TKE values are significant within the fog layer and are also captured by the model. However, Meso-NH overestimates TKE near the ground, as confirmed by additional measurements from a 3-m anemometer (shown later in Figure 6e). Overestimation of TKE in fog simulations - and more generally in stable layers - is a known issue (Zilitinkevich et al., 2008). According to Shao et al. (2025), improving the surface flux parameterization could be one way to improve the TKE representation by weakening the wind shear contributions. However, this is beyond the scope of the present study.

For IOP 11, Meso-NH's temperature and wind profiles are in fairly good agreement with observations until 04:00 UTC. Around 03:00 UTC, as the warm front approaches, the wind shifts southward and experiences a significant increase in TKE, which the model reproduces to some extent. Beyond 03:00 UTC, however, while the increase in wind intensity and TKE is reproduced, discrepancies become more pronounced. Consequently, this study focuses specifically on the fog formation and development of IOP 11 up to 03:00 UTC.

Overall, Meso-NH quite accurately reproduces the thermodynamic (temperature and vapour mixing ratio) and dynamical (wind intensity and direction) profiles, while overestimating TKE, especially near the surface, for both IOPs 6 and 11. This validation is crucial for the subsequent microphysical analysis, as highlighted by Costabloz et al. (2024), which shows that the microphysical profile is closely related to the thermodynamic state of the fog.

The next step is therefore to categorize the fog into different phases based on its adiabatic state, using the methodology developed by Costabloz et al. (2024) and Dione et al. (2023), which integrates ground instruments and remote sensing data.

4 Fog phases determination

Fog analysis is categorized according to the phases of fog evolution (Dione et al., 2023; Costabloz, 2024). The initial development phase begins when the horizontal visibility falls below 1000 m, indicating the formation of a thin fog layer on the ground, associated with stable conditions. This is followed by a transition phase, during which the fog layer becomes thick enough to radiate sufficiently in the longwave spectrum, warming the surface. The fog then evolves into a well-mixed layer. The third phase, called the adiabatic phase, corresponds to the life cycle of this well-mixed fog until approximately 30 minutes before dissipation, followed by the final dissipation phase, which lasts until approximately 30 minutes after the fog has lifted.

To characterize the thin-to-thick transition phase, we follow the methodology developed by Costabloz et al. (2024); Dione et al. (2023) applying specific thresholds to characterize:

- The inversion destruction near the surface with a TKE at 3 m exceeding 0.1 $m^2.s^{-2}$ (Dhangar et al., 2021).
- The shift of the cooling area to the top of the fog layer with a negative vertical temperature gradient within the 10-50 m layer.
- The fog becoming optically thick with an absolute net longwave radiation difference ($|LWnet|$) lower than 5 Wm^{-2} that can also be described by an LWP greater than 15 $g.m^{-2}$ according to Costabloz et al. (2024) and a CTH greater than 110 m according to Wærsted et al. (2017).

Fields are previously averaged over a 10-minute sliding window to reduce variability, except for TKE which has a 30-minute temporal resolution.

Before determining the phases, we first compare the characteristic fields between observations and simulations, and between the two IOPs.

Figure 6 shows the evolution of these quantities for IOP 6 and IOP 11, comparing observations with simulations. In IOP 6, visibility decreases abruptly in both observations and simulation due to advective contributions, whereas in IOP 11, the decrease is more gradual. After its formation, the evolution of fog during IOP 6 follows a classical radiation fog life cycle in both series: visibility drops to a minimum before gradually increasing, similar to the case previously studied by Mazoyer et al. (2019). In contrast, for IOP 11, the model temporarily dissipates the fog around 23:00 UTC, while the observations maintain it, with subsequent differences in evolution attributed to the approaching warm front.

Some discrepancies in the LW fields result from variations in fog formation between observations and simulations for both IOP 6 (before 22:00 UTC) and IOP 11 (before 00:00 UTC). However, as the fogs develop and become optically thick for LW radiation, LW downwelling (LWD) approaches LW upwelling (LWU) values, resulting in quasi-similar intensities in both observations and model outputs. For IOP 6, the simulated LWnet is higher in absolute terms than the observed values, which could be due to errors other than clouds, such as water vapour absorption or aerosol concentration. Notably, the radiative effect of aerosols is not included in these simulations.

Before the fog and during its formation, the observed and simulated TKE are negligible for both IOPs. During fog development, TKE increases, but simulated values systematically overestimate observations, as highlighted above.

The mean temperature gradient (dT/dz) between 10 m and 50 m reflects the air mass stability. For IOP 6, this gradient quickly becomes negative, due to fog formation via advection, even faster in the simulation than in the observations. In contrast, the period with a positive gradient lasts longer for IOP 11. During fog development, the thermal gradient is negative in all data sets, but the simulated values are higher than the observed ones, which explains the overestimation of simulated TKE by thermal production.

Regarding the fog cloud, the model systematically overestimates LWP (Fig. 6i,j), as highlighted above. In contrast, CTHs are fairly well reproduced. This may be due to excessive water production or insufficient depletion. The periods of overestimation of the LWP coincide fairly well with those of overestimation of the TKE. This may indicate a vicious circle, i.e. excess TKE produces excessive droplet activation, and excess droplets limit the negative temperature gradient, favouring the thermal production of TKE.

Focusing on the thin-to-thick transition phase, the different thresholds are shown in Fig. 6m,n: as expected, the observed ones are in good agreement with Figs. 9 and 10 of Costabloz et al. (2024); Dione et al. (2023), with slight discrepancies. These differences arise from two main factors: firstly, Costabloz et al. (2024) calculated the temperature gradient between 50 m and 25 m, whereas we used the mean gradient between 50 m and 10 m; secondly, we employed different sliding average methods with 30-minute and 10-minute windows. As seen in Fig.6, observational data fluctuate (e.g., LWP or temperature gradient), meaning small computational differences can lead to significant differences in threshold determination. Additionally, the slow evolution of some variables (e.g., LWnet, CTH, and TKE) emphasizes the importance of accurate threshold selection.

For both IOPs, in the observations, the earliest threshold is given by LWnet and the latest by CTH, with more than a four-hour gap for IOP 6, and a two-hour gap for IOP 11. In simulations, due to the rapid formation by advection in IOP 6, the TKE, thermal gradient and LWP thresholds coincide almost immediately after formation, while the CTH and LWnet thresholds are reached after three and four hours, respectively. For IOP 11, the beginning of the thin-to-thick transition period is also given by the TKE and LWP thresholds, with the last threshold coming from the thermal gradient. Table 2 summarizes the different phases for IOP 6 and IOP 11, highlighting both observed and modeled characteristics. Phase durations are relatively similar between model and observation, confirming the correct thermodynamic and dynamic representation, except for the adiabatic phase of IOP 11, which is affected by the approaching warm front.

https://doi.org/10.5194/egusphere-2025-5528
Preprint. Discussion started: 4 December 2025

As the times defined by the thresholds applied to the different parameters do not coincide, the first and last times are used to define the thin-to-thick transition phase. Now that the phases in the fog's life cycle have been determined, the validation of microphysics according to these phases can be addressed.

5 Microphysical evaluation

This section focuses on the microphysical evaluation of the simulated fog events, based on a comparison with the vertical profiles of LWC and Nc, as derived from CDP observations under the tethered balloon. First, we briefly evaluate the representativeness of the CDP range diameter measurements by comparing the reflectivity derived from the CDP with the reflectivity measured by the BASTA radar. Next, we analyse the microphysical vertical profiles and DSDs throughout the fog events and group them according to their respective evolutionary phases. Finally, we conduct a budget study to shed light on the microphysical processes involved throughout the fog life cycle, and to improve our understanding of the discrepancies between observations and simulation.

We note that a precise description of the observed vertical profile of LWC throughout the fog life cycle has been carried out in Costabloz et al. (2024), and a subsequent paper will hopefully analyze the observed Nc profiles and DSDs.

5.1 Representativeness of the CDP range diameter measurements

In this section, we first revisit Figure 2 and compare the reflectivity derived from the CDP with that measured by the BASTA radar. This enables us to evaluate the range of droplet diameters present for each IOP. Since reflectivity depends on the sixth-order moment of the DSD, it is particularly sensitive to the largest droplets. The lower reflectivity derived from the CDP than from the BASTA suggests that there may have been droplets larger than the 50 μm upper limit of the CDP's measurement range. However, BASTA sometimes appears to underestimate reflectivity for reasons that must be explored. Also, note that, without proper instrumentation to measure droplets larger than 50 μm, it is impossible to determine their relative importance to Nc and LWC, since reflectivity is highly sensitive to even a small number of large droplets.

Figure 2 shows that, during IOP 6, the reflectivity derived from the CDP is lower than that derived from the BASTA, particularly between 02:00 and 05:00 UTC. However, during IOP 11, there is good agreement between the reflectivity derived from CDP observations under the tethered balloon and BASTA measurements during the formation and thin-to-thick transition phases (until 02:14 UTC).

This suggests that, despite numerous reverse reflectivity profiles reported by the CDP being a potential signature of the collision-coalescence process, droplets larger than 50 μm in diameter during the formation and thin-to-thick transition phases of IOP 11 may not have been so numerous. However, more of them may have been produced during IOP 6.

As LIMA has no specific drizzle parameterization, as in Khairoutdinov and Kogan (2000), no drizzle is modeled in IOP 6 (confirmed by the low simulated reflectivity value). However, a very low rain content is modeled in IOP 11. Bearing this in mind, the simulated droplet size shown later falls within the range of the CDP measurements. This enables a meaningful comparison to be made between the model and the observations within this diameter range.

https://doi.org/10.5194/egusphere-2025-5528
Preprint. Discussion started: 4 December 2025

5.2 General comparison of the vertical profiles

Figures 7 and 8 compare the vertical profiles of LWC and Nc measured by the CDP aboard the tethered balloon at Charbonnières with those simulated by the model for IOP 6 and IOP 11, respectively. For IOP 6, the tethered balloon was not launched during the formation phase, preventing an evaluation of the model at this stage. During the thin-to-thick transition, the vertical profiles of both LWC and Nc are initially quite vertically uniform. However, as the transition progresses, higher observed LWC values shift upward within the fog layer after 00 UTC. The model overestimates LWC values during this phase, particularly in the second part of the transition, where simulated LWC reaches 0.45 $g{\cdot}m^{-3}$ compared to 0.3 $g{\cdot}m^{-3}$ observed near the fog top, contributing to the LWP overestimation. Similarly, observed Nc also shift upward, with peak values reaching 200 cm^{-3} near the fog top. The model, in contrast, shows a too uniform Nc profile around 100 cm^{-3} and fails to capture the higher concentrations observed at the fog top. During the adiabatic phase, observed LWC peaks near the fog top, with maximum values around 0.3 $g{\cdot}m^{-3}$, while the model continues to overestimate it, reaching 0.45 $g{\cdot}m^{-3}$, but a bit less than during the previous phase. After 0400 UTC, simulated LWC decreases and becomes more aligned with observations, although still slightly overestimated. Observed Nc also peaks at the fog top, reaching up to 500 cm^{-3}, likely due to droplet activation driven by radiative cooling. However, the model still produces too vertically uniform Nc profiles, with less pronounced activation at the top and mainly stronger values closer to the ground. Concentrations increase significantly throughout the fog layer during the adiabatic phase, more than 200 cm^{-3}. The decrease in concentration modeled towards 0500 UTC is likely due to advection, as confirmed by the subsequent budget analysis. Some of the profiles observed deserve to be described in more detail. For example, the descent at 03:00 UTC shows low LWC/Nc values associated with high reflectivity (Fig. 2a), suggesting enhanced coalescence and sedimentation. At 06:00 UTC during ascent, a strong LWC/Nc peak with reasonable reflectivity was observed in the upper part, possibly due to intense top-mixing. During the dissipation phase, observed LWC decreases and becomes more homogeneously distributed, while the model continues to overestimate LWC in the upper fog layers. Nc concentrations rise again towards the top in the observations, but the model overestimates the fog depth, while producing correct values in the first 150 m. In summary for IOP 6, the observed LWC and Nc profiles evolve similarly. Initially, they are uniform profiles, followed by an increase at the fog top. However, the model consistently overestimates LWC over the fog layer and produces overly uniform Nc profiles by overestimating Nc near the ground and underestimating the peaks at the fog top.

For IOP 11, the focus is primary on the formation and thin-to-thick transition phases. During the formation phase, both observations and simulations show a reverse LWC gradient, with maximum values (0.2 $g{\cdot}m^{-3}$) near the surface, and low Nc concentrations below 100 cm^{-3}, underestimated by the model. During the thin-to-thick transition phase, observed LWC and Nc vertical profiles become nearly vertically uniform, although the reverse gradient persists at 0200 UTC for LWC. A short-lived but significant Nc peak (300 cm^{-3}) is measured near the fog top at 0100 UTC, but overall Nc concentrations remain relatively low. The model strongly overestimates LWC in this phase, with values exceeding 0.5 $g{\cdot}m^{-3}$ near the top, compared to observed values closer to 0.2 $g{\cdot}m^{-3}$. The model also simulates an Nc gradient, with peaks (300 cm^{-3}) near the fog top - this was not seen in IOP 6 simulation. As the transition continues, LWC remains overestimated in the model, and simulated Nc becomes more vertically uniform.

https://doi.org/10.5194/egusphere-2025-5528
Preprint. Discussion started: 4 December 2025

In summary, for IOP 11, the model overestimates the LWC across the entire fog depth, particularly in the upper part of the fog layer, significantly more than in IOP 6. For the two cases, this overestimation is consistent with the overestimation of LWP, and more pronounced in IOP 11 than IOP 6, while the CTH is correctly reproduced (Fig. 6). On the other hand, simulated Nc values fall within the correct order of magnitude, i.e. $\sim$ [10-250] cm^{-3}. Notably, the model now avoids the systematic Nc overestimation reported in previous studies (Mazoyer et al., 2017; Ducongé et al., 2020). This improvement stems from the refined droplet activation parameterization introduced by Vié et al. (2024), particularly the consideration of continuous growth of existing cloud droplets by condensation.

For IOP 11, the LWC overestimation is consistent with the overestimated radar reflectivity values, whereas for IOP 6, the LWC overestimation in the fog layer contrasts with the previously noted underestimation of reflectivity. This suggests a potential issue with the DSD (including drizzle), as previously noted.

It is worth noting that the low concentrations observed during IOP 11 may be influenced by oceanic air masses and the presence of large hygroscopic sea salt particles. These factors may limit activation under low supersaturation conditions (Barahona et al., 2010), while still allowing for vapour deposition and LWC growth.

To gain a better understanding of the model's limitations, we will analyse the vertical profiles of LWC and Nc, aggregated by phase, to provide an overview of how the DSD vertical profile evolves. This will then be used to track the microphysical processes involved in the observations, as well as those identified in the previous thermodynamic analysis. We will then compare these with the processes involved in the simulation. This will help us to explain the processes behind the model misrepresentation.

5.3 Vertical profiles and DSDs aggregated by phase

Figures 9 and 10 present the vertical profiles of temperature, LWC, Nc, aggregated over the different fog phases, and the corresponding DSD, aggregated over different vertical layers, for IOP 6 and IOP 11 respectively. This section aims to assess the representativeness of phase aggregation with regard to the vertical profiles of temperature, LWC and N, in order to further evaluate DSD evolution.

During IOP 6, some discrepancies are observed between the temperature profiles measured by the HATPRO radiometer and those simulated by the model, across all fog phases. In the thin-to-thick transition phase, the model exhibits a warm bias near the surface, which had already been identified in previous comparisons with radiosoundings. In contrast, during the adiabatic phase, the radiometer indicates a cold bias relative to the simulation, even more marked during the dissipation phase. These inconsistencies may stem partly from limitations inherent to radiometric retrievals near the surface, where the vertical resolution is coarse and the radiative transfer assumptions may be less accurate. Nonetheless, despite these uncertainties, the overall trends in the temperature profiles remain almost consistent between observations and simulations. Specifically, they reveal the formation and vertical growth of a well-mixed adiabatic layer during the transition from the thin to thick layer, and throughout the dissipation phase. Regarding LWC and Nc, IOP 6 exhibits significant variability during the thin-to-thick transition due to differences in the sub-phase before and after 00 UTC. Aggregating the 23 vertical profiles smooths out these changes, resulting in a nearly uniform LWC and a slight increase in Nc with height. While the model captures the structure, it overestimates the LWC at all levels, which is consistent with the wet bias identified in Fig. 3. It also overestimates the Nc close to the surface. However, a comparison with the observed standard deviation shows a tendency to underestimate Nc in the upper layer, which is consistent with Fig. 7. During the adiabatic phase (16 observed vertical profiles) and the dissipation phase (3 observed vertical profiles), both the observed and the simulated profiles show a peak in LWC at the fog top, with similar vertical evolution. The observed Nc peaks at the top, while the modeled Nc remains uniform vertically.

During IOP 11, the simulation tends to be slightly too cold during the formation phase, which is also consistent with radiosounding data. In both observations and simulations, the temperature profiles capture the erosion of the near-surface stable layer during the formation phase, followed by the development of a well-mixed adiabatic layer during the thin-to-thick transition. During the formation phase, aggregation of the five observed profiles reveals a surface LWC peak and a vertically uniform Nc, both with low dispersion. While the model captures the profile shapes, it overestimates LWC due to the cold bias and significantly underestimates Nc. During the thin-to-thick transition, aggregation of the three observed profiles shows less dispersion than in IOP 6, probably due to the less numerous profiles. LWC tends towards a quasi-uniform profile, while retaining a surface peak; Nc remains vertically uniform. The model displays strong dispersion and overestimates both LWC and Nc, particularly at the fog top.

In summary, and in line with previous analyses, aggregating Nc and LWC by phase confirms that, while Meso-NH captures the relative vertical profile of LWC quite well, it systematically overestimates the values during the thin-to-thick transition and the adiabatic phase for both IOPs. Thermodynamic biases contribute to this overestimation. It also produces Nc profiles that are too homogeneous vertically. This phase-based aggregation approach is considered reliable. The vertical profile of DSD is now described. DSD is also aggregated by depth into three vertical layers, each 75 m in height.

During the thin-to-thick transition phase of IOP 6, the 10 μm diameter mode is firmly observed across the entire layer, which indicates that activation has occurred throughout. However, the concentration within this mode is higher at the top of the fog, in the [75-150] m layer. This is consistent with Nc evolution during the second sub-phase of the transition (Fig. 7), as well as with stronger activation at the top of the fog layer, which is probably the result of radiative cooling. Conversely, small- to medium-sized droplets (up to 30 μm in diameter) are more prevalent in the bottom layer, which is likely due to substantial condensational growth. This is consistent with LWC evolution during the initial sub-phase of the transition (Fig. 7). Consequently, the observed aggregated DSD increases in size towards larger diameters at the bottom. Droplets larger than 30 μm in diameter are recorded in the bottom layer, which suggests gravitational collision-coalescence, and is consistent with the CDP reflectivity analyses shown in Fig. 2.

During the adiabatic and dissipation phases, the 10 μm activation mode remains well established throughout the entire layer, and more pronounced at the top. This suggests continuous activation within the fog layer due to adiabatic motions, and to radiative cooling at the top of the fog layer. The concentration of small- to medium-sized droplets evolves slightly vertically, and large droplets are now present throughout the fog layer, with an increased concentration towards the bottom. A key finding of this analysis is the relative stability of small- to medium-sized droplets (up to 30 μm in diameter) in the lower fog layer compared to the upper layers throughout the adiabatic and dissipation phases, despite an increase in LWC towards the top. A $dM/dlogD$ (with M the mass) representation (not shown) reveals that differences in LWC are predominantly driven by the

https://doi.org/10.5194/egusphere-2025-5528
Preprint. Discussion started: 4 December 2025

10 μm mode diameter. This is consistent with the very high concentration of small droplets compared to small- to medium-sized ones (several orders of magnitude) in the $dN/dlogD$ representation. This indicates that activation and direct subsequent condensation growth are of primary importance in representing fog microphysics.

A comparison with the DSD from the model shows that, during the thin-to-thick transition phase, the modeled DSD increases in size towards larger diameters at the bottom, representing a similar range of droplet diameters to that observed. However, the model misses the 10 μm mode and overestimates the concentration of small- to medium-sized droplets. During the adiabatic and dissipation phases, the model still struggles to represent the 10 μm diameter mode separately in the lower layer. It also misses the biggest droplets, particularly near the ground, explaining the underestimation of the radar reflectivity. Contrary to observations, the DSD depicts a decrease in the concentration of small- to medium-sized droplets in the bottom layer, despite the absence of large droplets. The increase in LWC towards the top is related to the enlargement of the DSD. The DSDs presented in Fig. 9 and 10 include the distribution that the model would have with the observed LWC and Nc values represented by the pink line. This is to isolate the error arising from the Gamma law when considering a single-mode. For IOP 6, these distributions provide a more accurate representation of the 10 μm mode, particularly near the fog top. However, they fail to capture the enlargement of the DSD towards larger droplets. Using a single mode for droplets prevents a second mode from forming in large droplets.

The DSD observed during IOP 11 shows that only the 10 μm diameter activation mode is present from top to bottom, during the formation phase. This is present at a lower concentration than in IOP 6. The concentration of small- to medium-sized droplets increases through the bottom layer, probably due to condensation growth caused by surface cooling. Meanwhile, the 10 μm diameter activation mode persists: during the thin-to-thick transition phase, this mode is present throughout the fog layer again. However, a second, very distinct mode appears in small- to medium-sized droplets, affecting even the larger ones. This mode broadens towards the bottom. This is consistent with the reverse reflectivity profile, previously observed during the thin-to-thick transition phase of IOP 11, suggesting collisional growth. The $dM/dlogD$ representation (not shown) reveals that the differences in LWC are predominantly driven by small- to medium-sized droplets and large droplets. Unlike IOP 6, condensation growth and collision coalescence appear to have a stronger impact. The differences in IOP for condensation growth over small, small-to-medium, and large droplets could be explained by differences in Nc concentration. As Nc is lower in IOP 11, there should be less competition for vapor deposition. This may be due to a lower concentration of aerosols, or larger ones. Indeed, sea salt could have been present during IOP 11.

Comparisons with the DSD from the model show that, due to the concentration of droplets being too small during the IOP 11 formation phase, the DSD enlarges towards very large droplets, which should favor modeling rain formation. Consequently, small and medium droplets are missed, as shown by the pink DSDs produced with the observed LWC and Nc applied to the gamma law. During the thin-to-thick transition phase, the DSD enlarges towards the bottom, as observed. However, due to the excess in LWC and Nc, the modeled DSD appears too large compared to the observations. Due to structural limitations, LIMA is unable to accurately represent the bimodal nature of the DSD. This may explain why the 10 μm diameter mode is misrepresented during IOP 11 near the bottom, and why the largest droplets (>30 μm in diameter) are overestimated.

https://doi.org/10.5194/egusphere-2025-5528
Preprint. Discussion started: 4 December 2025

We will now use a budget analysis to gain a better understanding of the processes contributing to the faults we have just described. Our focus is on identifying the causes of excessive LWC during the thin-to-thick and adiabatic phases, as well as the absence of an Nc vertical gradient, which we explore through a model budget analysis.

5.4 Analysis of the microphysical processes

Figures 11 and 12 present the simulated budgets of rc and Nc for IOPs 6 and 11, respectively. They show the components corresponding to the dynamical (advection and turbulence) and microphysical (evaporation/condensation, hereafter referred to as adjustment, and sedimentation/deposition) processes for the two variables. For Nc, the activation is also considered, as well as in the total tendency. Note that the contributions of self-collection and break-up to the Nc budget are not shown, as they are negligible. Unlike the Nc budget, turbulence is not presented separately in the rc budget (but it is included in the total contribution), as it applies to the conservative variable of total non-precipitating water, rather than to the mixing ratios of vapour and cloud water separately. In addition to improving the understanding of the microphysical characteristics, the budget analysis is also used to establish links with model biases identified in previous sections.

As previously shown, the simulated formation phase of IOP 6 is very short, which is consistent with advective formation; rc and Nc production are driven by transport. Conversely, during the IOP 11 radiative formation, rc production is driven by saturation adjustment, corresponding to a local process. This production is partly offset by sedimentation. Nc is only produced by activation, most likely due to radiative cooling. However, this is offset by transport and evaporation. Consequently, the total Nc tendency is close to zero, resulting in a lack of Nc (Fig. 10c). The main causes are the dryness inducing evaporation and the excessive stable temperature profile, which prevents a positive turbulence term.

During the thin-to-thick transition phase, advection and turbulence are important sources of rc and Nc at the fog top, but mainly act as sink terms for both IOPs inside the fog layer. This may reflect the upward transport associated with the formation of weak convective movements during fog development. Saturation adjustment acts as a sink term for both rc and Nc at the fog top due to evaporation, and as an important source for rc by condensation just below the fog top due to radiative cooling.

Within the fog layer, transport can act as a source or sink term for Nc, but always as a sink term for rc. When the two are opposite, this may be due to the transport of a greater number of droplets with a lower liquid water content. Condensation also acts as a source term of rc within the fog layer, albeit less intensely than at the fog top. The condensation process is responsible for the excessive rc production. For IOP 6, this excess is due to high humidity, as shown in Fig. 3b and 4b. For IOP 11, the bias is due to the temperature being too low in the first hundred meters since formation. These biases contribute to the rapid vertical development of the fog, reinforcing the cooling at the fog top. This could generate excessive top-down buoyancy in the fog layer, favouring fog development. Excessive cooling at the fog top also favours the activation and excess of Nc, which is significantly larger for IOP 11 than for IOP 6. Since the transition phase, deposition acts as a sink term just above the ground. Logically, sedimentation acts as a sink term for rc and Nc at the fog top, and a source term within the fog layer. The sedimentation process mainly contributes to the shift towards larger droplets in the DSD when moving towards the bottom for both IOPs (Fig. 9 and Fig. 10). This shift is in agreement with observations for IOP 6, while it is largely overestimated for IOP 11 due to excess of rc within the fog layer. Considering the total tendencies of this phase for both IOPs, rc is primarily

https://doi.org/10.5194/egusphere-2025-5528
Preprint. Discussion started: 4 December 2025

produced at the top due to advection, and just below the top by condensation. Meanwhile, Nc is primarily produced at the fog top by transport and activation. These effects contribute to fog development.

During the adiabatic phase, which concerns only IOP 6 in terms of comparison to observations, the behavior of the processes is quite similar to that of the thin-to-thick transition phase, albeit more pronounced. We have seen that a major shortcoming of the simulation comes from an overestimation of Nc near the ground, with an overestimation of droplets between 10 and 20 μm. This could be due to the activation process of Nc, which remains positive in the first 150 meters throughout this phase and is not entirely consumed by the evaporation. This overestimation of activation is thought to be a consequence of the overestimation of the TKE near the ground, as seen in Fig.6e. Conversely, concentrations of droplets between 25 and 40 μm, albeit lower, are missing. As previously mentioned, this is due to the single-mode assumption in DSD, as illustrated by the pink line in Fig. 9j,k,l. An inaccurate representation of the DSD shape could lead to incorrect sedimentation behavior.

During the dissipation phase of IOP 6, transport processes are primarily responsible for the sinks of rc and Nc. The same causes mentioned previously produce the same misrepresentation of DSD.

6 Discussion

Comparing simulated fog using the two-moment microphysical scheme LIMA in Meso-NH revealed that both the fog life cycle and the cloud top height were well simulated, but also highlighted discrepancies between the observations and the simulations. For IOP 6 and IOP 11, biases in the microphysical representation were identified and are now discussed.

First, there is overestimation of LWC during the thin-to-thick transition phase, which can lead to a rapid phase shift (Boutle et al., 2018), and during the adiabatic phase, which can delay fog dissipation (Bott, 1991; Zhang et al., 2014). This also leads to excessive radiative cooling, and subsequent strong activation at the fog top, as well as top-down buoyancy. The overestimated LWC is consistent with the overestimation of LWP for a well-estimated CTH. This is mainly due to thermodynamic biases: a wet bias during IOP 6 and a cold bias during IOP 11.

Other sensitivity tests (not shown) using IOP 6 were conducted to mitigate LWC by reinforcing potential sink terms, particularly sedimentation. Firstly, reducing the aerosol loading slightly decreased Nc with little effect on the LWC or the Nc profile. However, the reduction may not have been strong enough. Secondly, increasing the deposition velocity from 2 cm/s to 6 cm/s (Katata, 2014) halved both the LWC and Nc values in the fog layer, but Nc remained homogeneous on the vertical. It should be noted that an accurate deposition velocity or a parametrization considering TKE, for example, could be a key avenue for improving the absolute values of LWC. During SOFOG3D, Price (2025) measured dew deposition fluxes and reported typical values of 50 g.m^{-2}.h^{-1}. Our simulation produce close values with 20 g.m^{-2}.h^{-1} for dew deposition flux and 35 g.m^{-2}.h^{-1} for gravitational settling flux. This is consistent with the previous comparison of observations and simulations conducted during LANFEX by Vié et al. (2024).

Furthermore, the impact of mixing at the fog top, particularly the related top-down mixing, should be better quantified, as highlighted by Yang and Gao (2020). Indeed, LWC is overestimated during IOP 6, whereas the upper layer is either quite wet (in the thin-to-thick transition phase) or dry (in the adiabatic phase) (Fig. 6 and 7). Using instrumentation dedicated to radiation, such as pyrgeometers under tethered balloons, may help to understand the radiative budget at the top of the fog layer, and better quantify top radiative cooling and its impact on top-down mixing.

The second issue concerns the misrepresentation of the DSD, primarily during the adiabatic phase of IOP 6: the absence of droplets with diameters greater than 20 microns explains the underestimation of radar reflectivity, despite the overestimation of LWP. This issue did not arise for IOP 11, as the excess LWC allows the full range of droplet sizes to be represented. Failing to detect the largest droplets, as occurred in IOP 6, could result in inaccurate sedimentation modeling, leading to excessive LWC. It could also disrupt the activation processes, according to Bott (1991), by conserving a strong sink term for supersaturation, which may be particularly important at the fog top. This could also affect radiative cooling.

LIMA assumes a generalized gamma DSD, with fixed values for the shape parameters alpha and nu. Thus, a simple option to modify the DSD is to use different values for these two parameters. Using $\alpha = 1$ and $\nu = 3$ for the DSD, instead of the other way around, provided a better fit for the DSD (not shown), yielding reflectivity values closer to the observations. However, this did not correct the Nc profile. A global fit to the entire SOFOG3D dataset could provide interesting insights; however, there is no doubt that these shape parameters would depend on aerosol loading and fog phases, which would make reaching a consensus difficult. Adding a third moment to the distribution, such as reflectivity, might allow for a better representation (Milbrandt and Yau, 2005). Ultimately, the use of bin schemes, as in Lábó and Geresdi (2016), should definitely help to constrain the shape of the DSD.

Our study has shown that the misrepresentation of DSD is partly due to the single-mode assumption. A bimodal DSD is a common feature in fog, as observed in both IOP 11 and 6, and has been cited in previous studies (Choularton et al., 1981; Gerber, 1991). Whether this second droplet mode serves as a critical LWC sink remains an open question. There have been numerous observations of drizzle in fog (Okita, 1962; Wendisch et al., 1998; Frank et al., 1998; Gultepe et al., 2007), including an observational stratocumulus campaign with specific drizzle instrumentation and measurements as described in VanZanten et al. (2005). The DSD distribution on the CDP diameter range was very close to that of fog. During IOP 6, vertical Doppler velocities of up to 0.3 $\mathrm{m.s^{-1}}$ downwards (not shown) were associated with high reflectivity values (-15 dBZ). However, the fall velocity of a 50 μm diameter droplet (the upper threshold of the CDP) does not exceed 0.1 $\mathrm{m.s^{-1}}$. Additionally, the reflectivity derived from the CDP exhibited lower values than the BASTA ones during this IOP. A comparable underestimation of reflectivity was also observed for IOP 14 in Bell et al. (2022), indicating the absence of larger droplets. According to Matrosov et al. (2004), drizzle typically occurs when reflectivity values are higher than -20 dBZ. Such values appear to have been reached for both IOPs. Therefore, everything seems to indicate the presence of large droplets (greater than 50 μm), which the instruments were unable to observe. In fact during SOFOG3D, a MPS (Meteorological Particle Spectrometer) from Droplet Measurement Technologies had measured particle size distribution ranging from 25 μm to 125 μm. However, no validation has yet been performed during the campaign. Very early results suggest that droplets larger than 50 μm were present throughout, occasionally growing to sizes of up to 200 μm when reflectivity reached -20 dBZ. Further analysis and measurement of droplets larger than 50 μm in diameter may help to determine the effect of drizzle on reflectivity, LWC and Nc in fog.

There are two main hypotheses that seek to explain the bimodal DSD, but no consensus has been reached. The first hypothesis involves mass transfer from the first droplet mode to the second via gravitational and turbulent collisional coalescence (Xue

https://doi.org/10.5194/egusphere-2025-5528
Preprint. Discussion started: 4 December 2025

et al., 2008; Zhao et al., 2013) or Ostwald ripening (Wendisch et al., 1998). The second hypothesis suggests that giant CCN, such as large sea-salt particles, are activated in the second DSD mode (Richter et al., 2021), which could also form from unactivated large hydrated particles (Frank et al., 1998). Meanwhile, the activation of aerosol particles from the accumulation mode would create the first DSD mode. This scenario is consistent with IOP 11, which shows a bimodal DSD and a maritime influence on aerosol loading. However, considering the DSD broadening from top to bottom during IOP 11, it seems unlikely that the effects of aerosols and Ostwald ripening are confined to the lowest level. Consequently, more weight could be given to the gravitational collision-coalescence theory for this specific case.

Currently, the LIMA scheme does not have the capability to model a bimodal DSD and two-mode activation. Although efforts have been made to implement the Khairoutdinov and Kogan (2000) parameterization, which is better suited to drizzle formation than the original rain parameterization in LIMA, little success has been achieved using it. Modifications would be required to correctly position the drizzle mode in fog observations. Nevertheless, three-class parameterizations for warm microphysics, representing droplets, drizzle and rain could fill this gap, as demonstrated in Sant et al. (2013). In a similar way, the microphysics scheme of Saleeby and Cotton (2004), developed within the Regional Atmospheric Modeling System (RAMS), distinguishes between two categories of droplets: cloud1 (2–40 μm diameter) and cloud2 (40–80 μm diameter). Cloud1 results from CCN activation, while cloud2 forms through cloud1 autoconversion and giant CCN (type sea-salt) activation. Using a second droplet mode could potentially reduce supersaturation by providing more surface area for the first mode to grow. The authors also noted improved precipitation representation. Finally, a subgrid parameterization for drizzle, similar to that in Turner et al. (2012) for precipitation, could also be beneficial. Ultimately, a bimodal DSD representation could offer a better representation of the 10 μm diameter mode and radiative cooling at the fog top.

The third issue concerns the failure to capture the Nc gradient during the adiabatic phase, emphasizing the inaccurate DSD representation at the lowest levels. Regarding the Nc gradient at low concentrations near the bottom, IOP 6 exhibits this gradient, whereas IOP 11, which has a lower aerosol loading, shows a nearly uniform profile in the observations. However, numerous case studies observed in SOFOG3D have indicated the presence of this gradient during adiabatic phases (not shown). The differences between IOP 6 and IOP 11 should be explored further to assess potential links between this gradient and aerosol loading.

The homogeneous vertical profile of Nc during the transition and adiabatic phases may be due to intense low-level activation caused by overestimation of TKE or vertical velocities within the first 150 m, which limits the formation of the vertical gradient. The timing and location of low-level activation coincide with high simulated TKE values, which may enhance supersaturation. An experiment in which the contribution of TKE to activation was set to zero produced a vertical Nc profile with slightly decreasing concentrations towards the surface. However, the gradient still deviated significantly from the observed one. Furthermore, as discussed by Thouron et al. (2011), the maximum supersaturation diagnostic used in this study is highly effective in the case of convective clouds. However, this assumes that the turbulent structure responsible for supersaturation has a sufficiently long lifespan to allow maximum supersaturation to be reached, which cannot be guaranteed in fog. Furthermore, when considering fine vertical resolution, activation will occur in the mesh crossed by the turbulent structure. However, this is not necessarily where maximum supersaturation is reached. Diagnosing maximum supersaturation in fog can lead to

https://doi.org/10.5194/egusphere-2025-5528
Preprint. Discussion started: 4 December 2025

an overestimation of supersaturation, particularly where vertical velocities are strongest. New formulations for supersaturation calculations and activation in fog are emerging, such as Peterka et al. (2024), which does not directly use vertical velocity, Field et al. (2023), which weights the TKE contributing terms, and Martín Pérez et al. (2024), which considers a sink term for supersaturation of large CCN. It should be noted that considering the continuous growth of existing cloud droplets through condensation as a sink term for supersaturation, as we did, may be overly significant in cases where excess LWC is modeled, which is a frequent bias in fog modeling. This consideration arises from the use of maximum supersaturation diagnosis, whereas other methods, such as prognostic supersaturation (Thouron et al., 2011), calculate supersaturation explicitly. The latter approach has been shown to be useful as a reference in LES fog simulations (Vié et al., 2024). However, this requires very high spatial and temporal resolution.

7 Conclusion

The present study forms part of the SOFOG3D field campaign, which aims to improve the assessment of NWP models' ability to represent subgrid-scale microphysical processes in fog. It provides a detailed and consistent evaluation of the two-moment microphysical scheme LIMA on the life cycles of two fog events during IOPs 6 and 11. Two 48-h simulations were performed, on a 100-m horizontal grid model covering an area of 60 km by 40 km, centred on the main observation site. IOP 6 was an advective radiative fog, whereas IOP 11 was a radiative fog whose evolution was affected by an approaching warm front. This study leverages the unique SOFOG3D dataset, which combines vertical measurements from remote sensing instruments and a tethered balloon equipped with a cloud droplet probe, to derive LWC and droplet concentration. To the authors' knowledge, this is the first study to evaluate vertical microphysical profiles simulated with observations throughout the entire fog life cycle.

The first part of the study focused on evaluating the fog life cycle using remote sensing (BASTA radar, HATPRO radiometer, and WindCube wind lidar), as well as radiosoundings. Fog evolution as inferred from simulated reflectivity generally agrees with observations for both IOP 6 and IOP 11, particularly after formation for IOP 6 and until 04:00 UTC for IOP 11. Meso-NH quite accurately reproduces the thermodynamic (temperature and vapour mixing ratio) and dynamic (wind intensity and direction) characteristics of the fog, but develops a wet bias for IOP 6 and a cold bias for IOP 11, and overestimates the TKE profiles in both cases.

The second part of the study focused on determining the fog phases, including the thin-to-thick transition period, according to Dione et al. (2023); Costabloz et al. (2024). The model shows a fairly good agreement with the observations, enabling a microphysical evaluation.

The third part of the paper examined microphysical processes, by relying on a process budget from the model. Meso-NH successfully represents the reverse LWC profile during the formation phase of IOP 11, likely due to the sedimentation sink term and the presence of large simulated droplets (> 50 μm diameter). During the thin-to-thick transition phase of IOPs 6 and 11, the model captures the mixed LWC profile, but significantly overestimates it, mainly due to the previously highlighted thermodynamic biases. The model does not reproduce the vertical gradient of Nc for IOP 6, but does so for IOP 11, albeit with an overestimated concentration. During the adiabatic and dissipation phases of IOP 6, the model captures the LWC

https://doi.org/10.5194/egusphere-2025-5528
Preprint. Discussion started: 4 December 2025

profile shape but overestimates its values, which coincides with a drier layer above. However, it fails to reproduce the droplet concentration gradient. Budget analyses indicate that excessive low-level activation by turbulent motions may lead to the overproduction of droplets and the capture of water that is not used for droplet enlargement through coalescence. During the thin-to-thick transition, and the adiabatic and dissipation phases of IOP 6, the simulated DSD underestimates the droplet mode at 10 μm diameter, and a significant proportion of the largest droplets ($>$ 25 μm diameter). The largest droplets in the DSD at the bottom are not represented in the model. Consequently, the vertical evolution of the DSD differs between the model and the observation. This misrepresentation of DSD is partly due to the single-mode assumption, which limits the sedimentation process and contributes to the overestimation of the LWC.

Overall, the model provides a reasonable representation of both fog cases. However, some biases remain, such as the overestimation of LWC, and errors in droplet number concentration and size. While only two cases have been studied and our results are consistent with the literature — notably with regard to the modelled excess LWC — more case studies are definitely needed to confirm them. If these biases are confirmed in other cases, several approaches to improving the presented model can be considered, that have been presented in the discussion session.

The extensive SOFOG3D dataset would be valuable in achieving these goals, particularly in constraining the DSD shape more effectively using observed and radar-derived DSD moments (reflectivity and Doppler velocity). It could also provide further insight into mixing processes at the fog top. However, additional field campaigns are needed to evaluate radiative cooling at fog top, dew deposition velocity, particularly over different surface types, following the approach of Tav et al. (2018). These campaigns should also investigate the presence and impact of drizzle and its possible link to aerosol loading. Additional instrumentation, such as drizzle probes or radar Doppler spectral functionality (Kollias et al., 2011), would be highly beneficial. Finally, given the significant profile-to-profile variability observed within fog phases, robust evaluation of the mean state would require a much larger number of vertical profiles. To fully capture phase-dependent variability, a cloud radar with enhanced functionality would provide more continuous vertical information and measure vertical velocities and TKE inside the fog layer.

Code and data availability

All the data used in this study are hosted by the French National Center for Atmospheric Data and Services (AERIS) at the following links: https://doi.org/10.25326/89 (Canut, 2020), https://doi.org/10.25326/135 (Delanoë, 2020) and https://doi.org/10.25326/207 (Martinet, 2021). The CDP data files are being finalized for submission to the database. Data access can be provided by following the conditions fixed by the SOFOG3D project. The surface–atmosphere coupled model Meso-NH is open source and available at http://mesonh.aero.obs-mip.fr/ (Lac et al., 2018). The generated model output data supporting the results of this study are available from the corresponding author upon reasonable request.

Author contributions

MM, CL, FB, BV, TC, SA and MF prepared the manuscript and analyzed the data. TC processed in-situ data. MT and CL configured the model. MM performed the simulations. MF participated to the tethered balloon operations. FB was the PI of the SOFOG3D project, designed the field campaign and led the tethered balloon operations. CL was the PI of the high-resolution modeling task and co-led the process analysis task.

Competing interests

The authors declare that they have no conflict of interest.

Acknowledgments

The SOFOG3D field campaign was supported by Météo-France and ANR through grant AAPG 2018-CE01-0004. Data are managed by the French National Center for Atmospheric Data and Services (AERIS). The MWR deployment at Charbonière site was carried out thanks to support by the Köln University. MWR data have been made available, quality controlled and processed in the frame of CPEX-LAB (Cloud and Precipitation Exploration LABoratory, www.cpex-lab.de), a competence center within the Geoverbund ABC/J by acting 750 support of Ulrich Löhnert, Rainer Haseneder-Lind and Arthur Kremer from the University of Cologne. This collaboration is driven by the European COST actions ES1303 TOPROF and CA18235 PROBE.

Instruments	Vertical position	Measured Variable	Unit	Uncertainty	Temporal Resolution
Kipp and Sonnen Spectrometer	1 m	LWD/LWU	W/m^2	10 %	60 s
METEK Sonic Anemometer	3 m	TKE	m^2/s^2	20 %	30 min
Vaisala PWD22	3 m	Horizontal Visibility	m	15 %	15s
BASTA Cloud radar		Reflectivity (Z) CBH/CTH	dBZ m	0.5-2 dB	3s
HATPRO Radiometer		T LWP	K g/m^2	1.5K RMSE 20 g/m^2	10min 1s
XSENS Sensor		Altitude	m	5 m	10 s
Cloud Droplet Probe		LWC,Nc D = [2-50] μm	g/m^3, cm^{-3}	30 % , 20 %	1 s
Radiosounding		T, HU, V			
TSI SMPS	3 m	Dry aerosols particles distribution D = [10.6-493] nm	cm^{-3}	20 %	5 min
CCNC DMT	3 m	CCN concentration SS =[0.06-0.26] %	cm^{-3}	10%	20 min

Table 1. List of instruments used in this study

	Formation	Thin-to-thick transition	Adiabatic	Dissipation
IOP 6 OBS	20h37 - 21h22 (0h45)	- 01h34 (4h12)	- 08h54 (7h20)	- 09h54
MESO-NH	22h01 - 22h02 (0h01)	- 01h58 (3h56)	- 08h32 (6h34)	- 09h32
IOP 11 OBS	20h38 - 23h54 (3h16)	- 02h14 (2h20)	- 03h25 (1h11)	- 04h25
MESO-NH	20h34 - 00h28 (3h54)	- 03h11 (2h43)	- 07h40 (4h29)	- 08h40

Table 2. Time range of observed and modeled fog phases (in brackets the duration)

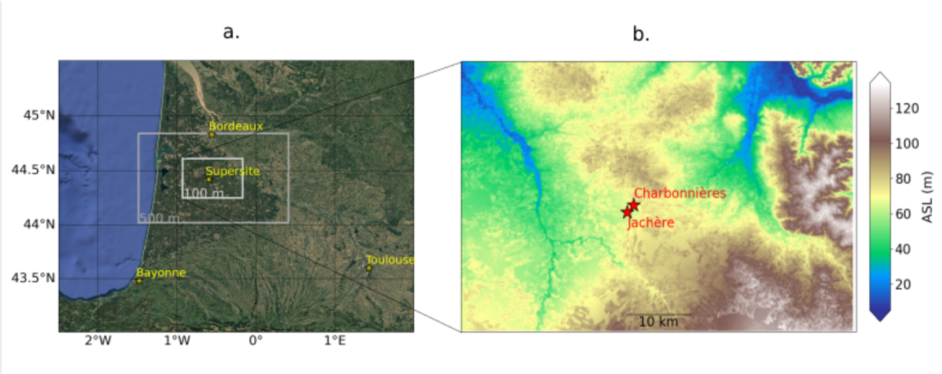

Figure 1. (a) Geographical location of the SOFOG3D supersite (©Google) and domains used for the 500 m simulation (dark grey rectangle) and the 100 m simulation (light grey rectangle). (b) Orography within the nested 100 m domain centred on the supersite station. The red stars correspond to the two measurement sites that make up the supersite.

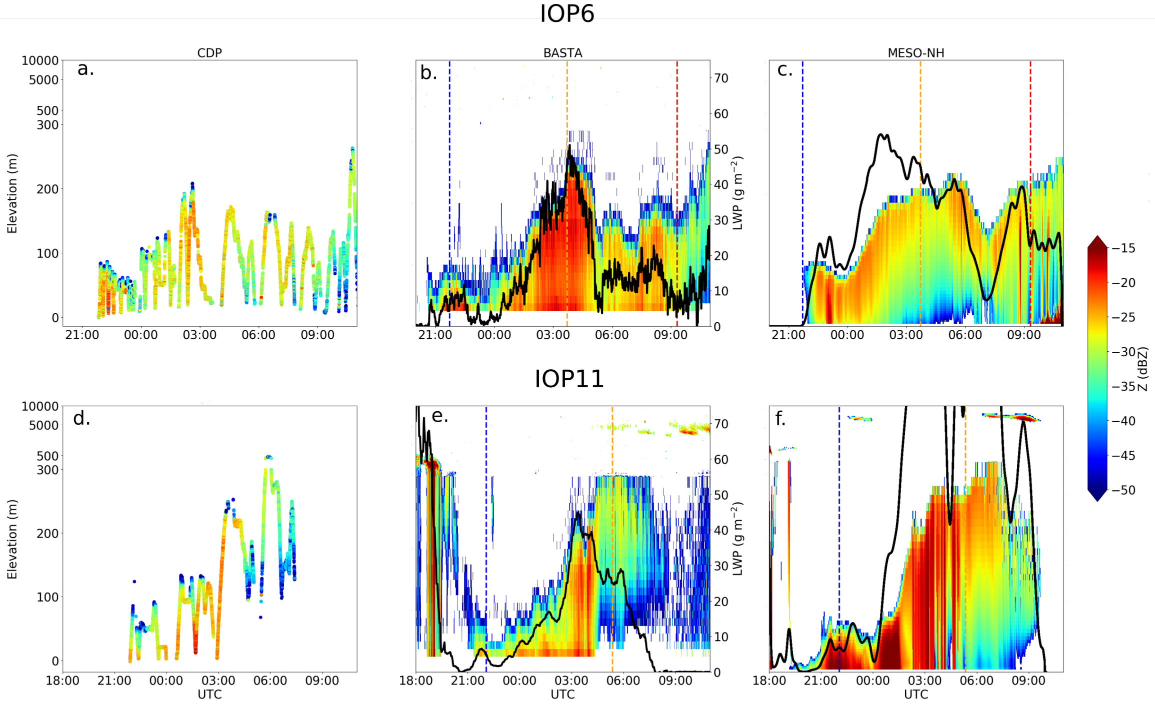

Figure 2. Temporal evolution of vertical profiles of radar reflectivity for IOP 6 (a,c) and IOP 11 (d,f), derived from CDP observations under the tethered balloon (a,d), from BASTA radar (b,e) and the 100 m simulation (c,f). Black lines represent the observed LWP from HATPRO (a,c) and the 100 m simulation (b,d). Vertical coloured dashed lines refer to the RS start time presented in Fig. 3. The vertical axis follows a logarithmic scale above 500 meters.

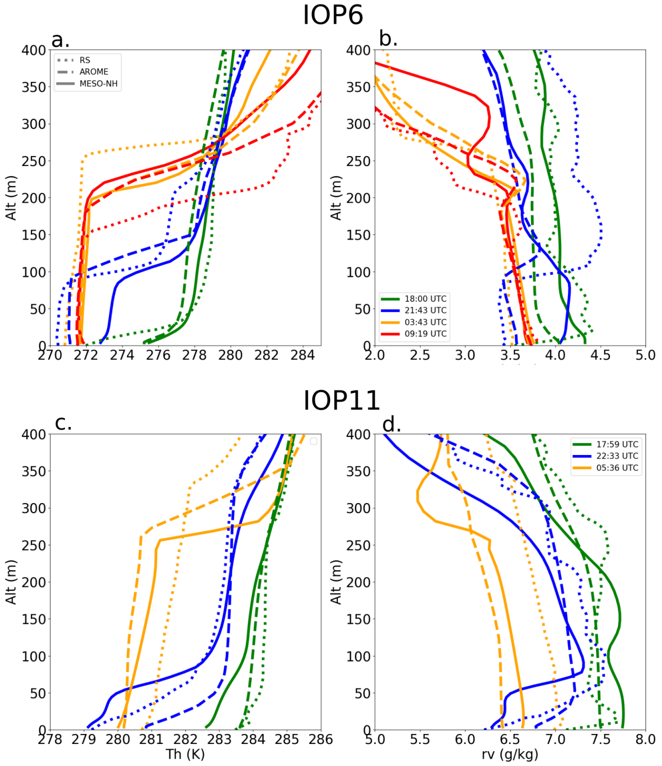

Figure 3. Vertical profiles of potential temperature (a,c) and vapour mixing ratio (b,d) at Charbonnières from radiosounding (dotted lines) and corresponding profile from AROME (dashed lines) and Meso-NH (plain lines) for different launch times 1800 UTC, 2143 UTC, 0343 UTC, and 0919 UTC for IOP 6 (a,b) and 1759 UTC, 2233 UTC, and 0536 UTC for IOP 11 (c,d). AROME fields correspond to temporally interpolated AROME analyses for IOP 6 and AROME-IFS forecasts for IOP 11. The launch times are reported in Fig. 2

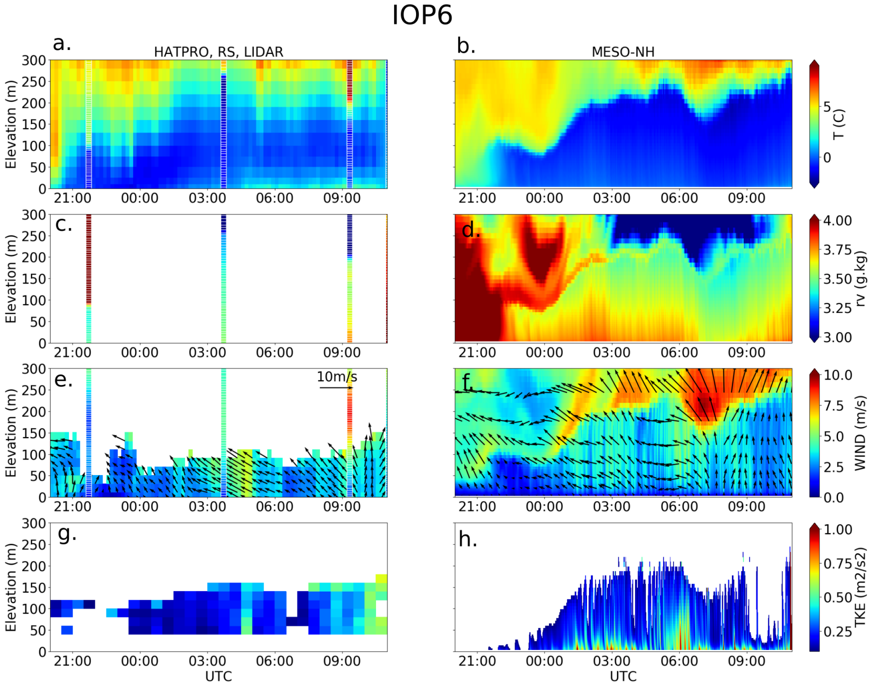

Figure 4. IOP 6: temporal evolution of vertical profiles of temperature (a,b), vapour mixing ratio (c,d), wind intensity and horizontal direction with north upward(e,f) and TKE (g,h) as measured by HATPRO (a), from RS (a,c,e), by lidar (e,g) and simulated by Meso-NH (b,d,f,h).

https://doi.org/10.5194/egusphere-2025-5528
Preprint. Discussion started: 4 December 2025

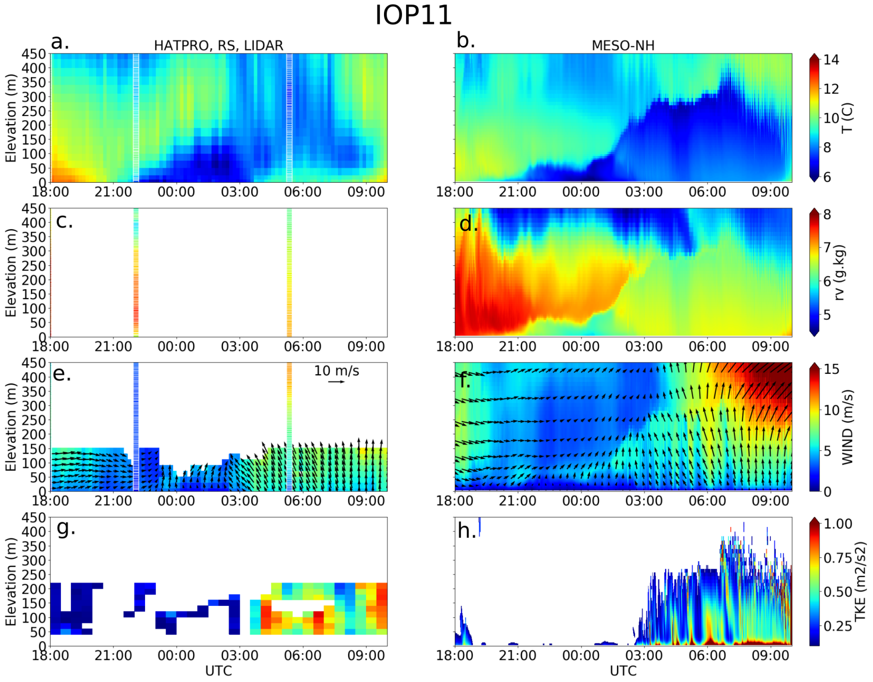

Figure 5. Same as Fig. 4 for IOP 11

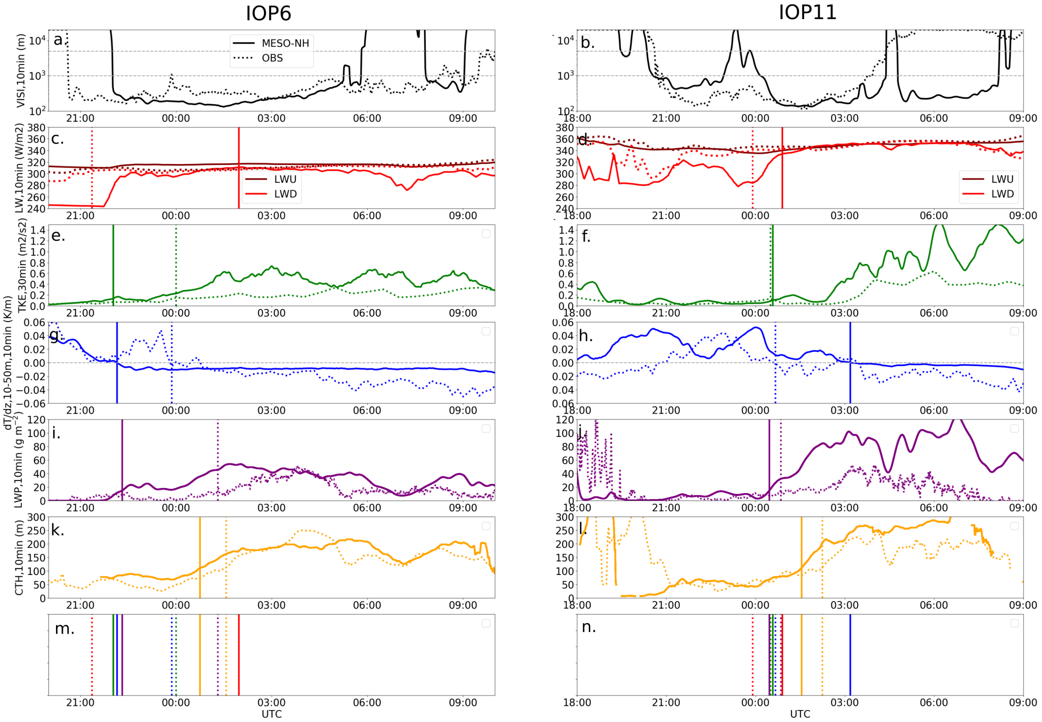

Figure 6. Temporal evolution of (a,b) visibility (c,d) downward (light red line) and upward (dark red line) longwave radiative fluxes, (e,f) TKE (green), (g,h) vertical gradient of temperature between 10 m and 50 m retrieved from the HATPRO microwave radiometer, (i,j) LWP retrieved from the microwave radiometer, (k,l) CTH retrieved from the BASTA cloud radar, at Charbonnières. (m,n) Thin-to-thick transition times estimated for Meso-NH (plain lines) and the observations (doted lines), using thresholds from the literature for all previous variables.

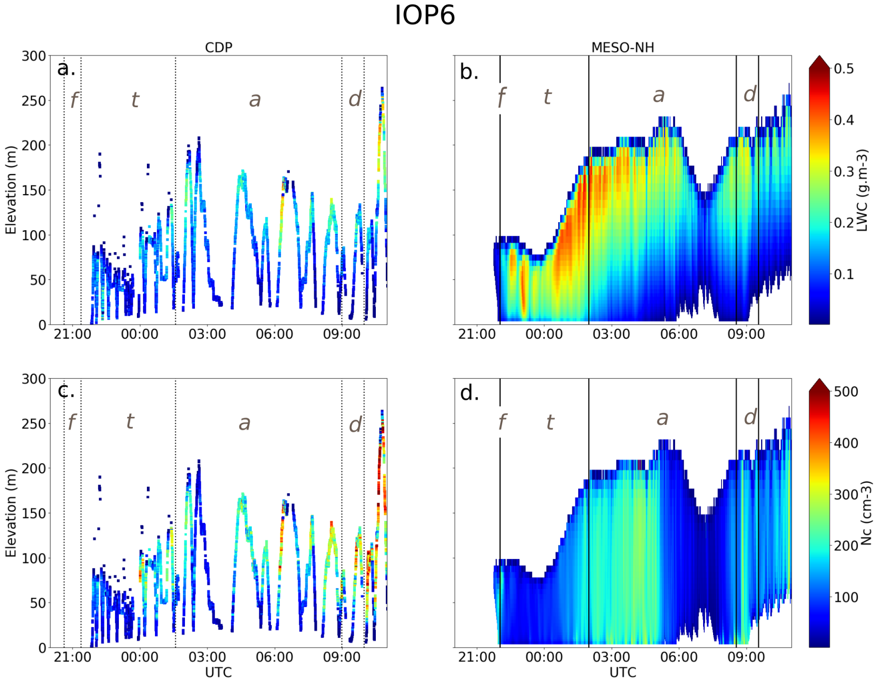

Figure 7. IOP 6: vertical profiles of LWC (a,b) and Nc (c,d) as measured by the CDP under the tethered balloon (a,c) and simulated by Meso-NH (b,d). The black vertical lines separate the fog phases, identified with grey letters (f: formation, t: thin-to-thick transition, a: adiabatic, d: dissipation).

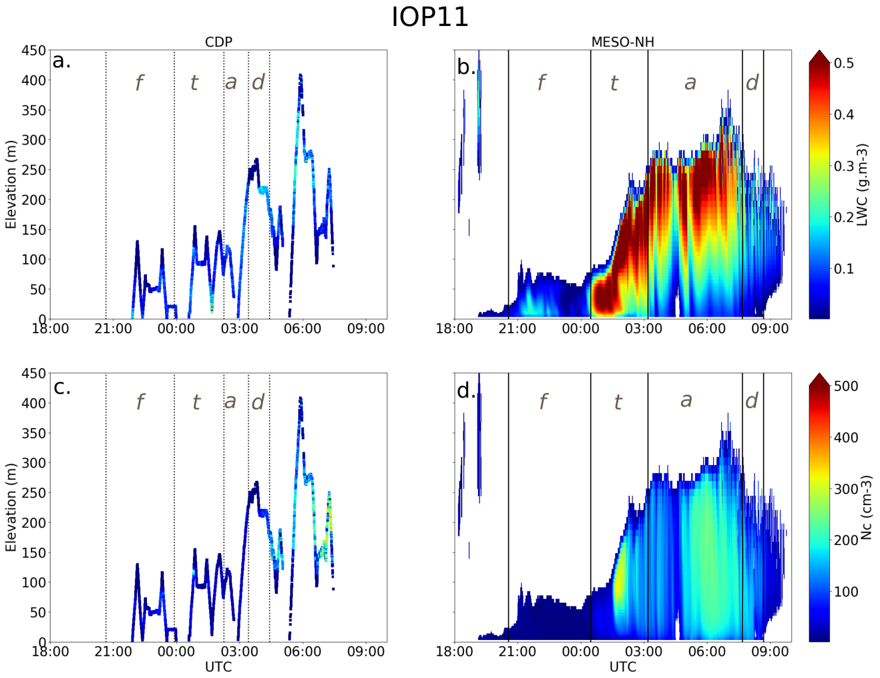

Figure 8. Same as Fig. 7 for IOP 11

https://doi.org/10.5194/egusphere-2025-5528
Preprint. Discussion started: 4 December 2025

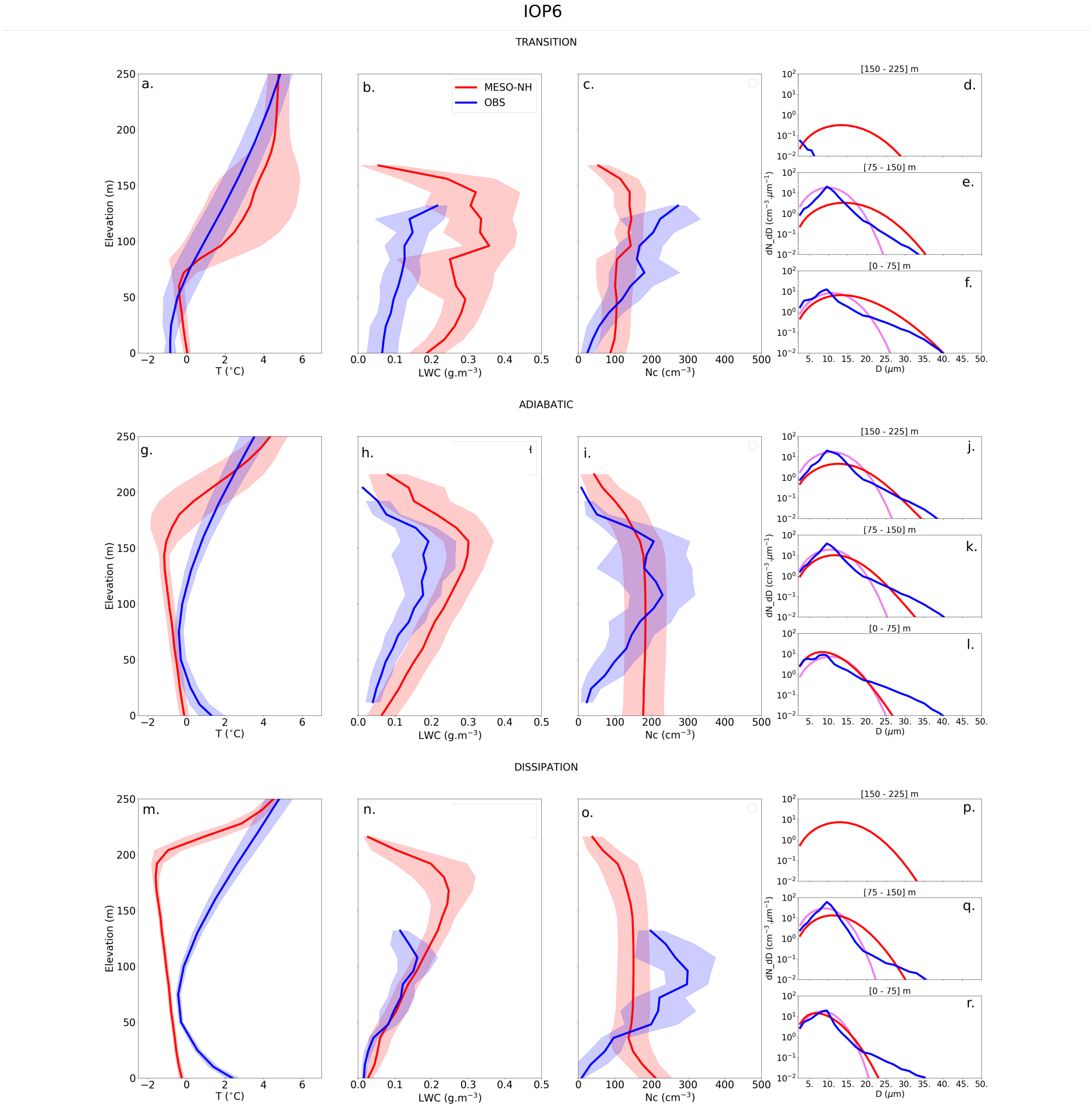

Figure 9. IOP 6: vertical profiles aggregated by phases (23 for the thin-to-thick transition for the first line, 16 for the adiabatic for the second line, 3 for dissipation for the third line) of: Observed and simulated (a,g,m) absolute temperature, (b,h,n) LWC, and (c,i,o) Nc. Panels on the right represent droplets distribution integrated over different layers. Model results are in continuous red and observation in dashed blue. For the DSDs, the pink line represents the distribution that the model would represent with the observed LWC and Nc. The envelops for the vertical profiles represent +- the standard deviation.

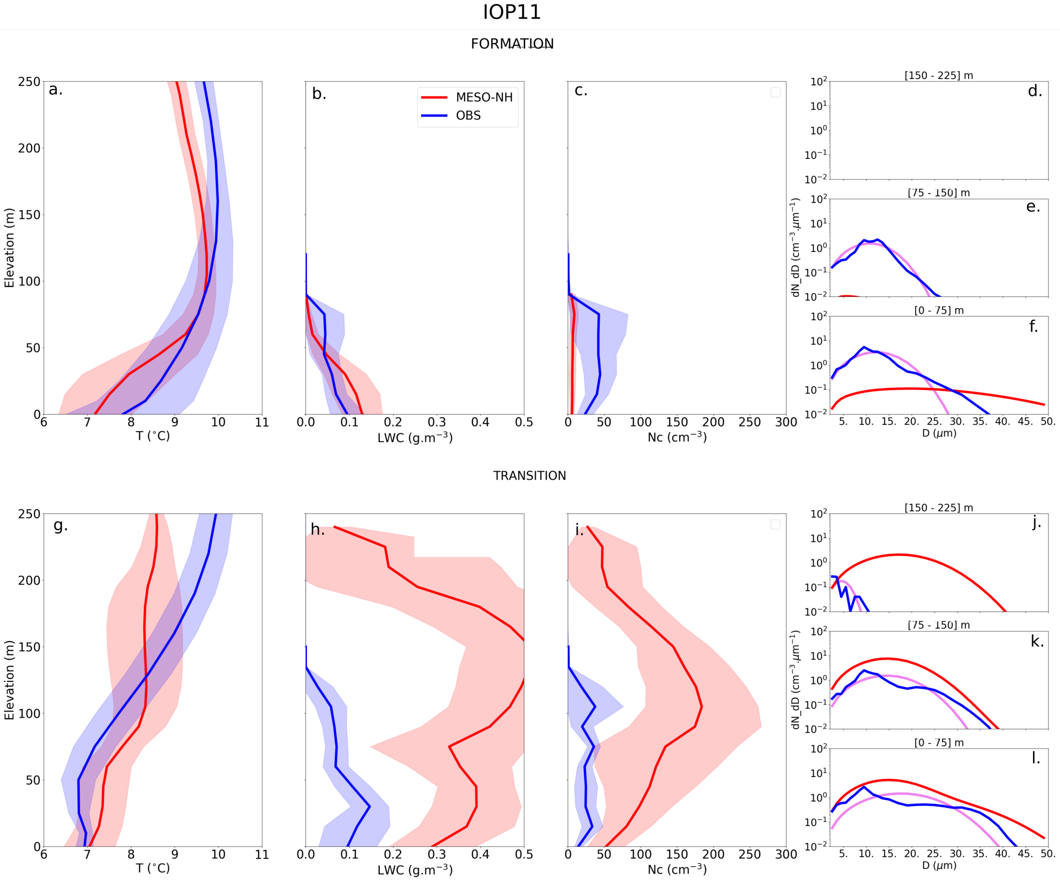

Figure 10. Same as Fig. 9 for IOP 11, but only for the 2 first periods, with 5 profiles aggregated for the formation phase for the first line and 3 for the thin-to-thick transition for the second line.

https://doi.org/10.5194/egusphere-2025-5528
Preprint. Discussion started: 4 December 2025

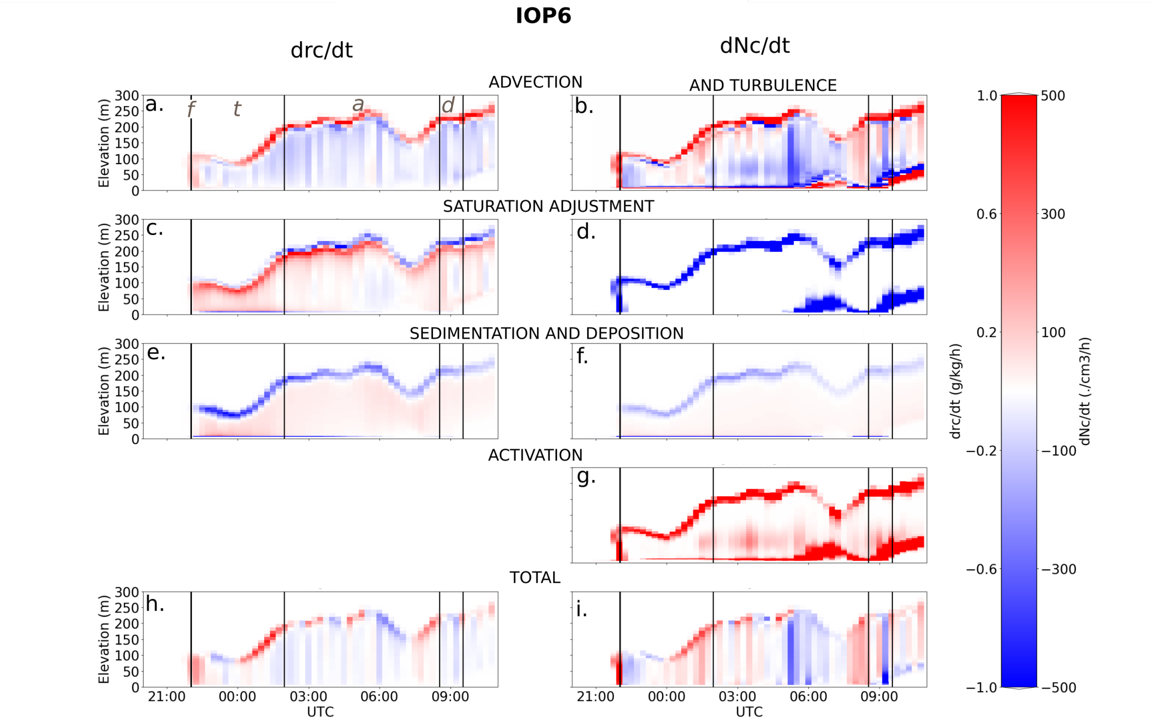

Figure 11. IOP 6: Vertical budget of rc and Nc during the fog life cycle: evolution (a: rc, e: Nc), due to advection (b: rc) and turbulence (f: Nc), saturation adjustment (c: rc, g: Nc), sedimentation and deposition (d: rc, h: Nc) and activation (i: Nc). The black vertical lines separate the fog phases, identified with grey letters (f: formation, t: thin-to-thick transition, a: adiabatic, d: dissipation).

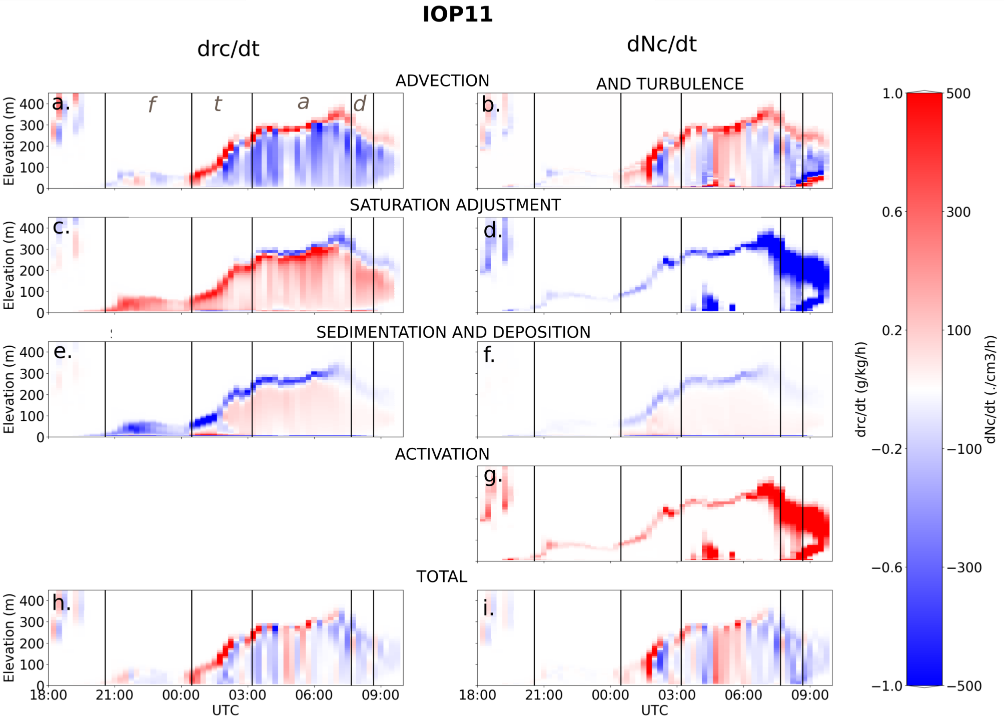

Figure 12. Same as Fig. 11 for IOP 11.

References

Antoine, S., Honnert, R., Seity, Y., Vié, B., Burnet, F., and Martinet, P.: Evaluation of an improved AROME configuration for fog forecasts during the SOFOG3D campaign, Weather and Forecasting, 38, 1605–1620, 2023.

Augros, C., Caumont, O., Ducrocq, V., Gaussiat, N., and Tabary, P.: Comparisons between S-, C-and X-band polarimetric radar observations and convective-scale simulations of the HyMeX first special observing period, Quarterly Journal of the Royal Meteorological Society, 142, 347–362, 2016.

Barahona, D., West, R., Stier, P., Romakkaniemi, S., Kokkola, H., and Nenes, A.: Comprehensively accounting for the effect of giant CCN in cloud activation parameterizations, Atmospheric Chemistry and Physics, 10, 2467–2473, 2010.

Beard, K. V. and Ochs III, H. T.: Warm-rain initiation: An overview of microphysical mechanisms, Journal of Applied Meteorology and Climatology, 32, 608–625, 1993.

Bell, A., Martinet, P., Caumont, O., Burnet, F., Delanoë, J., Jorquera, S., Seity, Y., and Unger, V.: An optimal estimation algorithm for the retrieval of fog and low cloud thermodynamic and micro-physical properties, Atmospheric Measurement Techniques, 15, 5415–5438, 2022.

Bergot, T. and Lestringant, R.: On the predictability of radiation fog formation in a mesoscale model: A case study in heterogeneous terrain, Atmosphere, 10, 165, 2019.

Berry, E. X. and Reinhardt, R. L.: An analysis of cloud drop growth by collection: Part I. Double distributions, Journal of Atmospheric Sciences, 31, 1814–1824, 1974.

Bott, A.: On the influence of the physico-chemical properties of aerosols on the life cycle of radiation fogs, Boundary-Layer Meteorology, 56, 1–31, 1991.

Bougeault, P. and Lacarrere, P.: Parameterization of orography-induced turbulence in a mesobeta–scale model, Monthly weather review, 117, 1872–1890, 1989.

Boutle, I., Price, J., Kudzotsa, I., Kokkola, H., and Romakkaniemi, S.: Aerosol–fog interaction and the transition to well-mixed radiation fog, Atmospheric Chemistry and Physics, 18, 7827–7840, 2018.

Boutle, I., Angevine, W., Bao, J.-W., Bergot, T., Bhattacharya, R., Bott, A., Ducongé, L., Forbes, R., Goecke, T., Grell, E., et al.: Demistify: an LES and SCM intercomparison of radiation fog., Atmospheric Chemistry & Physics Discussions, 2021.

Brousseau, P., Berre, L., Bouttier, F., and Desroziers, G.: Background-error covariances for a convective-scale data-assimilation system: AROME–France 3D-Var, Quarterly Journal of the Royal Meteorological Society, 137, 409–422, 2011.

Brousseau, P., Seity, Y., Ricard, D., and Léger, J.: Improvement of the forecast of convective activity from the AROME-France system, Quarterly Journal of the Royal Meteorological Society, 142, 2231–2243, 2016.

Burnet, F., Lac, C., Martinet, P., Fourrié, N., Haeffelin, M., Delanoë, J., Price, J., Barrau, S., Canut, G., Cayez, G., et al.: The SOuth west FOGs 3D experiment for processes study (SOFOG3D) project, in: EGU General Assembly Conference Abstracts, p. 17836, 2020.

Canut, G.: SOFOG3D_CHARBONNIERE_CNRM_TETHERED-BALLOON-MTO-10S_L2, https://doi.org/10.25326/89, 2020.

Choularton, T., Fullarton, G., Latham, J., Mill, C., Smith, M., and Stromberg, I.: A field study of radiation fog in Meppen, West Germany, Quarterly Journal of the Royal Meteorological Society, 107, 381–394, 1981.

Cohard, J.-M. and Pinty, J.-P.: A comprehensive two-moment warm microphysical bulk scheme. I: Description and tests, Quarterly Journal of the Royal Meteorological Society, 126, 1815–1842, 2000.

Colella, P. and Woodward, P. R.: The piecewise parabolic method (PPM) for gas-dynamical simulations, Journal of computational physics, 54, 174–201, 1984.

Contreras Osorio, S., Martín Pérez, D., Ivarsson, K.-I., Nielsen, K. P., de Rooy, W. C., Gleeson, E., and McAufield, E.: Impact of the Microphysics in HARMONIE-AROME on Fog, Atmosphere, 13, 2127, 2022.

Costabloz, T.: Profils verticaux des propriétés microphysiques du brouillard et leur évolution au cours de son cycle de vie, Ph.D. thesis, Université de Toulouse, 2024.

Costabloz, T., Burnet, F., Lac, C., Martinet, P., Delanoë, J., Jorquera, S., and Fathalli, M.: Vertical Profiles of Liquid Water Content in fog layers during the SOFOG3D experiment, Atmospheric Chemistry and Physics Discussions, 2024.

Cuxart, J.: When can a high-resolution simulation over complex terrain be called LES?, Frontiers in Earth Science, 3, 87, 2015.

Cuxart, J., Bougeault, P., and Redelsperger, J.-L.: A turbulence scheme allowing for mesoscale and large-eddy simulations, Quarterly Journal of the Royal Meteorological Society, 126, 1–30, 2000.

De Rooy, W. C., Siebesma, P., Baas, P., Lenderink, G., De Roode, S. R., De Vries, H., Van Meijgaard, E., Meirink, J. F., Tijm, S., and Van't Veen, B.: Model development in practice: a comprehensive update to the boundary layer schemes in HARMONIE-AROME cycle 40, Geoscientific Model Development, 15, 1513–1543, 2022.

Deardorff, J. W.: Stratocumulus-capped mixed layers derived from a three-dimensional model, Boundary-layer meteorology, 18, 495–527, 1980.

Delanoë, J., Protat, A., Vinson, J.-P., Brett, W., Caudoux, C., Bertrand, F., Parent du Chatelet, J., Hallali, R., Barthes, L., Haeffelin, M., et al.: BASTA: A 95-GHz FMCW Doppler radar for cloud and fog studies, Journal of Atmospheric and Oceanic Technology, 33, 1023–1038, 2016.

Delanoë, J.: SOFOG3D_CHARBONNIERE_LATMOS_BASTA-vertical_L2a, https://doi.org/10.25326/134, 2020.

Dhangar, N. G., Lal, D., Ghude, S. D., Kulkarni, R., Parde, A. N., Pithani, P., Niranjan, K., Prasad, D. S., Jena, C., Sajjan, V. S., et al.: On the conditions for onset and development of fog over New Delhi: an observational study from the WiFEX, Pure and Applied Geophysics, 178, 3727–3746, 2021.

Dione, C., Haeffelin, M., Burnet, F., Lac, C., Canut, G., Delanoë, J., Dupont, J.-C., Jorquera, S., Martinet, P., Ribaud, J.-F., et al.: Role of thermodynamic and turbulence processes on the fog life cycle during SOFOG3D experiment, Atmospheric Chemistry and Physics, 23, 15 711–15 731, 2023.

Dominutti, P. A., Renard, P., Vaïtilingom, M., Bianco, A., Baray, J.-L., Borbon, A., Bourianne, T., Burnet, F., Colomb, A., Delort, A.-M., et al.: Insights into tropical cloud chemistry in Réunion (Indian Ocean): results from the BIO-MAÏDO campaign, Atmospheric Chemistry and Physics, 22, 505–533, 2022.

Draxler, R. and Rolph, G.: HYSPLIT (HYbrid Single-Particle Lagrangian Integrated Trajectory) model access via NOAA ARL READY website (http://ready. arl. noaa. gov/HYSPLIT. php). NOAA Air Resources Laboratory, Silver Spring, MD, 25, 2010.

Ducongé, L., Lac, C., Vié, B., Bergot, T., and Price, J.: Fog in heterogeneous environments: the relative importance of local and non-local processes on radiative-advective fog formation, Quarterly Journal of the Royal Meteorological Society, 146, 2522–2546, 2020.

Egli, S., Maier, F., Bendix, J., and Thies, B.: Vertical distribution of microphysical properties in radiation fogs—A case study, Atmospheric Research, 151, 130–145, 2015.

Fathalli, M., Lac, C., Burnet, F., and Vié, B.: Formation of fog due to stratus lowering: An observational and modelling case study, Quarterly Journal of the Royal Meteorological Society, 148, 2299–2324, 2022.

Field, P. R., Hill, A., Shipway, B., Furtado, K., Wilkinson, J., Miltenberger, A., Gordon, H., Grosvenor, D. P., Stevens, R., and Van Weverberg, K.: Implementation of a double moment cloud microphysics scheme in the UK met office regional numerical weather prediction model, Quarterly Journal of the Royal Meteorological Society, 149, 703–739, 2023.

Frank, G., Martinsson, B., Cederfelt, S.-I., Berg, O., Swietlicki, E., Wendish, M., Yuskiewicz, B., Heintzenberg, J., Wiedensohler, A., Orsini, D., et al.: Droplet formation and growth in polluted fogs, Contributions to atmospheric physics, 71, 65–85, 1998.

Garcıa-Garcıa, F., Virafuentes, U., and Montero-Martınez, G.: Fine-scale measurements of fog-droplet concentrations: A preliminary assessment, Atmospheric research, 64, 179–189, 2002.

Gerber, H.: Supersaturation and droplet spectral evolution in fog, Journal of Atmospheric Sciences, 48, 2569–2588, 1991.

Ghude, S. D., Jenamani, R., Kulkarni, R., Wagh, S., Dhangar, N. G., Parde, A. N., Acharja, P., Lonkar, P., Govardhan, G., Yadav, P., et al.: WiFEX: walk into the warm fog over Indo-Gangetic Plain region, Bulletin of the American Meteorological Society, 104, E980–E1005, 2023.

Goodman, J.: The microstructure of California coastal fog and stratus, Journal of Applied Meteorology and Climatology, 16, 1056–1067, 1977.

Grabowski, W. W. and Wang, L.-P.: Growth of cloud droplets in a turbulent environment, Annual review of fluid mechanics, 45, 293–324, 2013.

Gultepe, I., Tardif, R., Michaelides, S. C., Cermak, J., Bott, A., Bendix, J., Müller, M. D., Pagowski, M., Hansen, B., Ellrod, G., et al.: Fog research: A review of past achievements and future perspectives, Pure and applied geophysics, 164, 1121–1159, 2007.

Hogan, R. J. and Bozzo, A.: A flexible and efficient radiation scheme for the ECMWF model, Journal of Advances in Modeling Earth Systems, 10, 1990–2008, 2018.

Katata, G.: Fogwater deposition modeling for terrestrial ecosystems: A review of developments and measurements, Journal of Geophysical Research: Atmospheres, 119, 8137–8159, 2014.

Khairoutdinov, M. and Kogan, Y.: A new cloud physics parameterization in a large-eddy simulation model of marine stratocumulus, Monthly weather review, 128, 229–243, 2000.

Kollias, P., Rémillard, J., Luke, E., and Szyrmer, W.: Cloud radar Doppler spectra in drizzling stratiform clouds: 1. Forward modeling and remote sensing applications, Journal of Geophysical Research: Atmospheres, 116, 2011.

Kumjian, M. R. and Prat, O. P.: The impact of raindrop collisional processes on the polarimetric radar variables, Journal of the Atmospheric Sciences, 71, 3052–3067, 2014.

Lábó, E. and Geresdi, I.: Study of longwave radiative transfer in stratocumulus clouds by using bin optical properties and bin microphysics scheme, Atmospheric Research, 167, 61–76, 2016.

Lac, C., Chaboureau, J.-P., Masson, V., Pinty, J.-P., Tulet, P., Escobar, J., Leriche, M., Barthe, C., Aouizerats, B., Augros, C., et al.: Overview of the Meso-NH model version 5.4 and its applications, Geoscientific Model Development, 11, 1929–1969, 2018.

Mackowski, D. W. and Mishchenko, M. I.: Calculation of the T matrix and the scattering matrix for ensembles of spheres, JOSA A, 13, 2266–2278, 1996.

Martín Pérez, D., Gleeson, E., Maalampi, P., and Rontu, L.: Use of CAMS near Real-Time Aerosols in the HARMONIE-AROME NWP Model, Meteorology, 3, 161–190, 2024.

Martinet, P.: SOFOG3D_CHARBONNIERE_CNRM_MWR-HATPRO-LWP_L2, https://doi.org/10.25326/207, 2021.

Martinet, P., Unger, V., Burnet, F., Georgis, J.-F., Hervo, M., Huet, T., Löhnert, U., Miller, E., Orlandi, E., Price, J., et al.: A dataset of temperature, humidity, and liquid water path retrievals from a network of ground-based microwave radiometers dedicated to fog investigation, Bulletin of Atmospheric Science and Technology, 3, 6, 2022.

Masson, V., Le Moigne, P., Martin, E., Faroux, S., Alias, A., Alkama, R., Belamari, S., Barbu, A., Boone, A., Bouyssel, F., et al.: The SURFEXv7. 2 land and ocean surface platform for coupled or offline simulation of earth surface variables and fluxes, Geoscientific Model Development, 6, 929–960, 2013.

Matrosov, S. Y., Uttal, T., and Hazen, D. A.: Evaluation of radar reflectivity–based estimates of water content in stratiform marine clouds, Journal of Applied Meteorology, 43, 405–419, 2004.

Mazoyer, M., Lac, C., Thouron, O., Bergot, T., Masson, V., and Musson-Genon, L.: Large eddy simulation of radiation fog: impact of dynamics on the fog life cycle, Atmospheric Chemistry and Physics, 17, 13 017–13 035, 2017.

Mazoyer, M., Burnet, F., Denjean, C., Roberts, G. C., Haeffelin, M., Dupont, J.-C., and Elias, T.: Experimental study of the aerosol impact on fog microphysics, Atmospheric Chemistry and Physics, 19, 4323–4344, 2019.

Mazoyer, M., Burnet, F., and Denjean, C.: Experimental study on the evolution of droplet size distribution during the fog life cycle, Atmospheric Chemistry and Physics, 22, 11 305–11 321, 2022.

Mazoyer, M., Ricard, D., Rivière, G., Delanoë, J., Riette, S., Augros, C., Borderies, M., and Vié, B.: Impact of mixed-phase cloud parameterization on warm conveyor belts and upper-tropospheric dynamics, Monthly Weather Review, 151, 1073–1091, 2023.

Milbrandt, J. and Yau, M.: A multimoment bulk microphysics parameterization. Part II: A proposed three-moment closure and scheme description, Journal of the atmospheric sciences, 62, 3065–3081, 2005.

Mlawer, E. J., Taubman, S. J., Brown, P. D., Iacono, M. J., and Clough, S. A.: Radiative transfer for inhomogeneous atmospheres: RRTM, a validated correlated-k model for the longwave, Journal of Geophysical Research: Atmospheres, 102, 16 663–16 682, 1997.

Noilhan, J. and Planton, S.: A simple parameterization of land surface processes for meteorological models, Monthly weather review, 117, 536–549, 1989.

Okita, T.: Studies of physical structure of fog, Journal of the Meteorological Society of Japan. Ser. II, 40, 39–50, 1962.

Peterka, A., Thompson, G., and Geresdi, I.: Numerical prediction of fog: A novel parameterization for droplet formation, Quarterly Journal of the Royal Meteorological Society, 2024.

Petters, M. and Kreidenweis, S.: A single parameter representation of hygroscopic growth and cloud condensation nucleus activity, Atmospheric Chemistry and Physics, 7, 1961–1971, 2007.

Pilié, R., Mack, E., Kocmond, W., Eadie, W., and Rogers, C.: The life cycle of valley fog. Part II: Fog microphysics, Journal of Applied Meteorology and Climatology, 14, 364–374, 1975.

Pinnick, R. G., Hoihjelle, D., Fernandez, G., Stenmark, E., Lindberg, J., Hoidale, G., and Jennings, S.: Vertical structure in atmospheric fog and haze and its effects on visible and infrared extinction, Journal of the Atmospheric Sciences, 35, 2020–2032, 1978.

Pinsky, M., Khain, A., and Shapiro, M.: Collision efficiency of drops in a wide range of Reynolds numbers: Effects of pressure on spectrum evolution, Journal of the atmospheric sciences, 58, 742–764, 2001.

Poku, C., Ross, A. N., Hill, A. A., Blyth, A. M., and Shipway, B.: Is a more physical representation of aerosol activation needed for simulations of fog?, Atmospheric Chemistry and Physics, 21, 7271–7292, 2021.

Price, J.: Radiation fog. Part I: observations of stability and drop size distributions, Boundary-layer meteorology, 139, 167–191, 2011.

Price, J.: Observations and quantification of fog droplet deposition made during the SOFOG3D campaign, Quarterly Journal of the Royal Meteorological Society, 151, e4908, 2025.

Price, J., Lane, S., Boutle, I., Smith, D., Bergot, T., Lac, C., Duconge, L., McGregor, J., Kerr-Munslow, A., Pickering, M., et al.: LANFEX: a field and modeling study to improve our understanding and forecasting of radiation fog, Bulletin of the American Meteorological Society, 99, 2061–2077, 2018.

Richter, D. H., MacMillan, T., and Wainwright, C.: A Lagrangian cloud model for the study of marine fog, Boundary-layer meteorology, pp. 1–20, 2021.

Roach, W., Brown, R., Caughey, S., Garland, J., and Readings, C.: The physics of radiation fog: I–a field study, Quarterly Journal of the Royal Meteorological Society, 102, 313–333, 1976.

Roberts, G. and Nenes, A.: A continuous-flow streamwise thermal-gradient CCN chamber for atmospheric measurements, Aerosol Science and Technology, 39, 206–221, 2005.

Rooy, W., Bruijn, C., Tijm, S., Neggers, R., Siebesma, P., and Barkmeijer, J.: Experiences with Harmonie at KNMI, HIRLAM Newsletter, 56, 21–29, 2010.

Saleeby, S. M. and Cotton, W. R.: A large-droplet mode and prognostic number concentration of cloud droplets in the Colorado State University Regional Atmospheric Modeling System (RAMS). Part I: Module descriptions and supercell test simulations, Journal of Applied Meteorology and Climatology, 43, 182–195, 2004.

Sant, V., Lohmann, U., and Seifert, A.: Performance of a triclass parameterization for the collision–coalescence process in shallow clouds, Journal of the atmospheric sciences, 70, 1744–1767, 2013.

Savijärvi, H., Arola, A., and Räisänen, P.: Short-wave optical properties of precipitating water clouds, Quarterly Journal of the Royal Meteorological Society, 123, 883–899, 1997.

Schwenkel, J. and Maronga, B.: Large-eddy simulation of radiation fog with comprehensive two-moment bulk microphysics: impact of different aerosol activation and condensation parameterizations, Atmospheric Chemistry and Physics, 19, 7165–7181, 2019.

Seity, Y., Brousseau, P., Malardel, S., Hello, G., Bénard, P., Bouttier, F., Lac, C., and Masson, V.: The AROME-France convective-scale operational model, Monthly Weather Review, 139, 976–991, 2011.

Shao, N., Lu, C., Li, Y., Jia, X., Wang, Y., Yin, Y., Zhu, B., Zhao, T., Liu, D., Niu, S., et al.: Impact of Improved Surface Flux Parameterization on Simulation of Radiation Fog Formation in the Yangtze River Delta, China, Journal of Geophysical Research: Atmospheres, 130, e2024JD042 345, 2025.

Tardif, R. and Rasmussen, R. M.: Event-based climatology and typology of fog in the New York City region, Journal of applied meteorology and climatology, 46, 1141–1168, 2007.

Tav, J., Masson, O., Burnet, F., Paulat, P., Bourrianne, T., Conil, S., Pourcelot, L., et al.: Determination of fog-droplet deposition velocity from a simple weighing method, Aerosol and Air Quality Research, 18, 103–113, 2018.

Thornton, J., Price, J., Burnet, F., and Lac, C.: Contrasting the evolution of radiation fog over a heterogeneous region in southwest France during the SOFOG3D campaign, Quarterly Journal of the Royal Meteorological Society, 149, 3323–3341, 2023.

Thouron, O., Brenguier, J.-L., and Burnet, F.: Supersaturation calculation in large eddy simulation models for prediction of the droplet number concentration, Geoscientific Model Development Discussions, 4, 3313–3337, 2011.

Turner, S., Brenguier, J.-L., and Lac, C.: A subgrid parameterization scheme for precipitation, Geoscientific Model Development, 5, 499–521, 2012.

Vaillancourt, P. A. and Yau, M.: Review of particle-turbulence interactions and consequences for cloud physics, Bulletin of the American Meteorological Society, 81, 285–298, 2000.

VanZanten, M., Stevens, B., Vali, G., and Lenschow, D.: Observations of drizzle in nocturnal marine stratocumulus, Journal of the atmospheric sciences, 62, 88–106, 2005.

Vié, B., Pinty, J.-P., Berthet, S., and Leriche, M.: LIMA (v1. 0): A quasi two-moment microphysical scheme driven by a multimodal population of cloud condensation and ice freezing nuclei, Geoscientific Model Development, 9, 567–586, 2016.

Vié, B., Ducongé, L., Lac, C., Bergot, T., and Price, J.: Importance of CCN activation for fog forecasting and its representation in the two-moment microphysical scheme LIMA, Quarterly Journal of the Royal Meteorological Society, 2024.

Wærsted, E. G., Haeffelin, M., Dupont, J.-C., Delanoë, J., and Dubuisson, P.: Radiation in fog: quantification of the impact on fog liquid water based on ground-based remote sensing, Atmospheric Chemistry and Physics, 17, 10 811–10 835, 2017.

Wendisch, M., Mertes, S., Heintzenberg, J., Wiedensohler, A., Schell, D., Wobrock, W., Frank, G., Martinsson, B. G., Fuzzi, S., Orsi, G., et al.: Drop size distribution and LWC in Po Valley fog, Contributions to atmospheric physics, 71, 1998.

Xue, Y., Wang, L.-P., and Grabowski, W. W.: Growth of cloud droplets by turbulent collision-coalescence, Journal of the Atmospheric Sciences, 65, 331–356, 2008.

Yang, Y. and Gao, S.: The impact of turbulent diffusion driven by fog-top cooling on sea fog development, Journal of Geophysical Research: Atmospheres, 125, e2019JD031 562, 2020.

Yau, M. K. and Rogers, R. R.: A short course in cloud physics, Elsevier, 1996.

Zhang, X., Musson-Genon, L., Dupont, E., Milliez, M., and Carissimo, B.: On the influence of a simple microphysics parametrization on radiation fog modelling: A case study during parisfog, Boundary-layer meteorology, 151, 293–315, 2014.

Zhao, L., Niu, S., Zhang, Y., and Xu, F.: Microphysical characteristics of sea fog over the east coast of Leizhou Peninsula, China, Advances in Atmospheric Sciences, 30, 1154–1172, 2013.

Zilitinkevich, S. S., Elperin, T., Kleeorin, N., Rogachevskii, I., Esau, I., Mauritsen, T., and Miles, M.: Turbulence energetics in stably stratified geophysical flows: Strong and weak mixing regimes, Quarterly Journal of the Royal Meteorological Society: A journal of the atmospheric sciences, applied meteorology and physical oceanography, 134, 793–799, 2008.